Title	GR-RMHD Simulations of Super-Eddington Accretion Flows onto a Neutron Star with Dipole and Quadrupole Magnetic Fields
Author(s)	Inoue, Akihiro; Ohsuga, Ken; Takahashi, R. Hiroyuki et al.
Citation	Astrophysical Journal. 2024, 977(1), p. 10
Version Type	VoR
URL	https://hdl.handle.net/11094/100423
rights	This article is licensed under a Creative Commons Attribution 4.0 International License.
Note	

The Astrophysical Journal, 977:10 (15pp), 2024 December 10 https://doi.org/10.3847/1538-4357/ad8885

GR-RMHD Simulations of Super-Eddington Accretion Flows onto a Neutron Star with Dipole and Quadrupole Magnetic Fields

Akihiro Inoue[1], Ken Ohsuga[2], Hiroyuki R. Takahashi[3], Yuta Asahina[2], and Matthew J. Middleton[4]

[1] Department of Earth and Space Science, Graduate School of Science, Osaka University, Toyonaka, Osaka 560-0043, Japan; ainoue@astro-osaka.jp

[2] Center for Computational Sciences, University of Tsukuba, 1-1-1 Ten-nodai, Tsukuba, Ibaraki 305-8577, Japan

[3] Department of Natural Sciences, Faculty of Arts and Sciences, Komazawa University, Tokyo 154-8525, Japan

[4] School of Physics & Astronomy, University of Southampton, Southampton, Southampton SO17 1BJ, UK

Received 2024 August 12; revised 2024 October 3; accepted 2024 October 16; published 2024 November 28

Abstract

Although ultraluminous X-ray pulsars (ULXPs) are believed to be powered by super-Eddington accretion onto a magnetized neutron star (NS), the detailed structures of the inflow–outflow and magnetic fields are still not well understood. We perform general relativistic radiation magnetohydrodynamics (GR-RMHD) simulations of super-Eddington accretion flows onto a magnetized NS with dipole and/or quadrupole magnetic fields. Our results show that an accretion disk and optically thick outflows form outside the magnetospheric radius, while inflows aligned with magnetic field lines appear inside. When the dipole field is more prominent than the quadrupole field at the magnetospheric radius, accretion columns form near the magnetic poles, whereas a quadrupole magnetic field stronger than the dipole field results in the formation of a belt-like accretion flow near the equatorial plane. The NS spins up as the angular momentum of the accreting gas is converted into the angular momentum of the electromagnetic field, which then flows into the NS. Even if an accretion column forms near one of the magnetic poles, the observed luminosity is almost the same on both the side with the accretion column and the side without it, because the radiation energy is transported to both sides through scattering. Our model suggests that galactic ULXP Swift J0243.6+6124 has a quadrupole magnetic field of 2×10^{13} G and a dipole magnetic field of less than 4×10^{12} G.

Unified Astronomy Thesaurus concepts: Radiative magnetohydrodynamics (2009); High energy astrophysics (739); Ultraluminous x-ray sources (2164); General relativity (641); Accretion (14); Neutron stars (1108)

1. Introduction

Ultraluminous X-ray sources (ULXs) are bright, point-like, and non-nuclear X-ray objects whose isotropic X-ray luminosity exceeds the Eddington luminosity for the stellar-mass black holes, $\sim 10^{39}$ erg s^{-1} (see recent reviews by P. Kaaret et al. 2017; S. N. Fabrika et al. 2021; A. King et al. 2023; C. Pinto & D. J. Walton 2023). Such a high X-ray luminosity suggests that they host either intermediate-mass black holes accreting at sub-Eddington rate (see, e.g., E. J. M. Colbert & R. F. Mushotzky 1999; K. Makishima et al. 2000; H. Matsumoto et al. 2001; J. M. Miller et al. 2003, 2004), stellar-mass black holes accreting at super-Eddington rate (see, e.g., A. R. King et al. 2001; K.-y. Watarai et al. 2001; J. Poutanen et al. 2007; J. C. Gladstone et al. 2009), and/or neutron stars (NSs) accreting at super-Eddington rate (see, e.g., M. M. Basko & R. A. Sunyaev 1976; A. R. King et al. 2001; M. Bachetti et al. 2014; A. A. Mushtukov et al. 2015). In some ULXs, coherent pulsations with a period of ∼1–10 s are detected (e.g., M. Bachetti et al. 2014; F. Fürst et al. 2016; G. L. Israel et al. 2017a, 2017b). Such ULXs are called ULX pulsars (ULXPs). It is widely accepted that the pulsations would be caused by the rotation of the magnetized NS (A. A. Mushtukov et al. 2018; A. Inoue et al. 2020). In order to reconcile the ULX luminosities, super-Eddington accretion onto the magnetized NS is required.

To model the super-Eddington accretion flows, general relativistic radiation magnetohydrodynamics (GR-RMHD) simulations are necessary. To date, many GR-RMHD simulations of super-Eddington accretion flows onto a black hole have been conducted (see, e.g., J. C. McKinney et al. 2014; A. Sadowski et al. 2014; H. R. Takahashi et al. 2016; A. Utsumi et al. 2022; A. Ricarte et al. 2023). These simulations showed that the numerical model can explain the observed features of the ULXs, such as the radiative luminosity, kinetic luminosity and radiation spectrum. However, only a few GR-RMHD simulations for the magnetized NS case have succeeded (H. R. Takahashi & K. Ohsuga 2017; D. Abarca et al. 2021; A. Inoue et al. 2023).

Due to interactions with the gas in the accretion disk, the closed magnetic field lines of the NS open up (see, e.g., K. Parfrey et al. 2016, and references therein). Additionally, within the radius where the magnetic pressure of the NS's magnetic field balances the radiation pressure of the accretion disk (the so-called magnetospheric radius), the gas flows onto the NS along its magnetic field lines. If the dipole magnetic field dominates over the other field components, accretion columns form near the NS's magnetic poles (H. R. Takahashi & K. Ohsuga 2017; D. Abarca et al. 2021). On the other hand, if the quadrupole magnetic field is predominant within the magnetosphere, a belt-like accretion flow appears around the NS's equator. We refer to such an accretion flow as an accretion belt. M. Long et al. (2007) have demonstrated the accretion belt around the star with quadrupole magnetic fields through magnetohydrodynamics (MHD) simulations. The accretion belt around the NS with a low accretion rate has also been confirmed by P. Das et al. (2022) through general relativistic magnetohydrodynamic (GR-MHD) simulations. In both cases, the accretion disks form outside the magnetospheric radius.

Observationally, in the ULXPs, it has been pointed out that the multipole magnetic field, which is stronger than the dipole magnetic field, exists near the NS surface. G. L. Israel et al. (2017b) suggested that a high luminosity of NGC 5907 ULX $\sim 10^{41}$ erg s^{-1} can be achieved if a multipole magnetic field with a strength of $\sim 10^{14}$ G exists (see, also K. Y. Eksi et al. 2015; N. Brice et al. 2021). L.-D. Kong et al. (2022) reported the cyclotron resonance scattering feature (CRSF) with a centroid energy of $E_{\rm cyc} \sim 150$ keV and a line width of $\sigma_{\rm cyc} \sim 20$–30 keV in the X-ray spectrum of Swift J0243.6+6124 using data from Insight-HXMT. The corresponding surface magnetic field strength is $\sim 2 \times 10^{13}$ G. This value is stronger than what is estimated based on the assumption that the NS has a dipole magnetic field (see, e.g., S. S. Tsygankov et al. 2018; V. Doroshenko et al. 2020; A. Inoue et al. 2023). Furthermore, motivated by the discovery of the CRSF in M51 ULX8 (M. Brightman et al. 2018), M. J. Middleton et al. (2019) also analyzed the X-ray spectra of M51 ULX8. From the spectral fitting, they obtained two solutions: $(E_{\rm cyc}, \sigma_{\rm cyc}) \sim (4.5\,{\rm keV}, 0.1\,{\rm keV})$ and $(E_{\rm cyc}, \sigma_{\rm cyc}) \sim (4.5\,{\rm keV}, 1\,{\rm keV})$. Such a CRSF would originate from the resonant scattering by electrons in the dipole magnetic field of 10^{12} G or by protons in the multipole magnetic field of 10^{15} G.

Although the existence of multipolar magnetic fields is frequently discussed, super-Eddington accretion flows onto an NS with multipolar magnetic fields are still not well understood. In this paper, we investigate the super-Eddington accretion flows around NSs with dipole and/or quadrupole magnetic fields using GR-RMHD simulations. We demonstrate that the observations, including CRSF, of Swift J0243.6+6124 can be explained by our model if the strength of the dipole magnetic field at the NS's magnetic pole is less than 4×10^{12} G and if that of the quadrupole field is around 2×10^{13} G. This paper is organized as follows: we will present the numerical methods in Section 2 and show the results in Section 3. Section 4 is devoted to the discussion of the NS's magnetic field structure in Swift J0243.6+6124. Finally, we give our conclusions in Section 5.

2. Method

We numerically solve the GR-RMHD equations in Schwarzschild polar coordinates (t, r, θ, ϕ) using the numerical code `UWABAMI` (H. R. Takahashi & K. Ohsuga 2017). Based on the moment formalism of the radiation field (K. S. Thorne 1981), this code adopts the M1 closure as the closure relation (C. D. Levermore 1984; Y. Kanno et al. 2013; A. Sadowski et al. 2013). In this closure, the radiation field is updated by solving the zeroth and first moment of the radiative transfer equation. The speed of light c and the gravitational constant G are normalized to 1 unless otherwise specified. Hereafter, spacetime and space components are represented by Greek and Latin suffixes, respectively.

2.1. Basic Equations

The equations for the time evolution of the GR-RMHD are given by (see, e.g., H. R. Takahashi et al. 2018)

$$\nabla_\mu(\rho u^\mu) = 0, \tag{1}$$

$$\nabla_\mu(T^{\mu\nu}) = G^\nu, \tag{2}$$

$$\nabla_\mu(R^{\mu\nu}) = -G^\nu, \tag{3}$$

$$\partial_t(\sqrt{-g}B^i) = -\partial_j\{\sqrt{-g}(b^i u^j - b^j u^i)\}, \tag{4}$$

where ρ is the proper mass density, u^μ is the four-velocity of the gas, B^i is the magnetic field vector in the laboratory frame, b^μ is the magnetic four-vector in the fluid frame, and $g = \det(g_{\mu\nu})$ is the determinant of the metric. The energy–momentum tensor of the ideal MHD is $T^{\mu\nu} = T_{\rm MA}{}^{\mu\nu} + T_{\rm EM}{}^{\mu\nu}$, where

$$T_{\rm MA}{}^{\mu\nu} = (\rho + e + p_{\rm gas})u^\mu u^\nu + p_{\rm gas}g^{\mu\nu}, \tag{5}$$

$$T_{\rm EM}{}^{\mu\nu} = b^2 u^\mu u^\nu + p_{\rm mag}g^{\mu\nu} - b^\mu b^\nu. \tag{6}$$

Here, e is the internal energy density, $p_{\rm gas} = (\Gamma - 1)e$ is the gas pressure ($\Gamma = 5/3$), and $p_{\rm mag} = b^2/2$ is the magnetic pressure in the fluid frame. In the M1 formalism, the energy–momentum tensor of the radiation field is expressed as (A. Sadowski et al. 2013)

$$R^{\mu\nu} = (\bar{E} + p_{\rm rad})u_{\rm R}{}^\mu u_{\rm R}{}^\nu + p_{\rm rad}g^{\mu\nu}. \tag{7}$$

Here, $\bar{E}$ is the radiation energy density, $p_{\rm rad} = \bar{E}/3$ is the radiation pressure in the radiation rest frame, and $u_{\rm R}{}^\mu$ is the four-velocity of the radiation rest frame. The interaction between the ideal MHD and radiation field is described by the radiation four-force,

$$\begin{aligned} G^\mu = &-\rho\kappa_{\rm abs}(R^{\mu\alpha}u_\alpha + 4\pi\hat{B}u^\mu) \\ &- \rho\kappa_{\rm sca}(R^{\mu\alpha}u_\alpha + R^{\alpha\beta}u_\alpha u_\beta u^\mu) + G_{\rm comp}{}^\mu, \end{aligned} \tag{8}$$

where $\kappa_{\rm abs} = 6.4 \times 10^{22}\rho T_{\rm e}^{-3.5}$ cm^2 g^{-1} is the opacity for free–free absorption, $\kappa_{\rm sca} = 0.4$ cm^2 g^{-1} is the isotropic electron scattering opacity, and $T_{\rm e}$ is the electron temperature. The blackbody intensity is given by $\hat{B} = aT_{\rm e}{}^4/4\pi$, where a is the radiation constant. In this study, we take thermal Comptonization into account (P. C. Fragile et al. 2018; A. Utsumi et al. 2022):

$$G_{\rm comp}{}^\mu = -\kappa_{\rm sca}\rho\hat{E}\frac{4k(T_{\rm e} - T_{\rm r})}{m_{\rm e}}u^\mu. \tag{9}$$

Here, $\hat{E}$ is the radiation energy density in the fluid frame, $T_r = (\hat{E}/a)^{1/4}$ is the radiation temperature, and $m_{\rm e}$ is the electron mass. We assume $T_{\rm e} = T_{\rm g}$ for simplicity, where $T_{\rm g}$ is the gas temperature. The gas temperature is calculated from $T_{\rm g} = \mu_{\rm w}m_{\rm p}p_{\rm gas}/(\rho k)$, where $m_{\rm p}$ is the proton mass, k is the Boltzmann constant, and $\mu_{\rm w} = 0.5$ is the mean molecular weight. We consider the subgrid model to mimic the mean-field dynamo proposed by A. Sadowski et al. (2015).

2.2. Numerical Models

We set the NS's mass and radius to $M_{\rm NS} = 1.4\,M_\odot$ and to $r_{\rm NS} = 10$ km, respectively. The rotation of the NS is ignored because the observed pulse period in ULXPs corresponding to the rotation period of the NS is 1–10 s, which is much longer than the Keplerian timescale, $\sim 10^{-2}$ s, even within $r \sim 100$ km. In the present paper, the axisymmetric system where the magnetic axis coincides with the rotation axis of the accretion disk is assumed. We fix the total magnetic field strength at the magnetic pole in the upper hemisphere to $B_{\rm tot} = B_{\rm dip} + B_{\rm qua} = 4 \times 10^{10}$ G. Here, $B_{\rm dip}$ and

Table 1

Parameters for Different Models

Parameters	f	(N_r, N_θ)	$r_{\rm out}$	ρ_0	$\dot{M}_{\rm in}$	$\dot{M}_{\rm out}$	$L_{\rm rad}$	$L_{\rm kin}$	$r_{\rm M}$
Unit			(km)	(g cm^{-3})	($\dot{M}_{\rm Edd}$)	($\dot{M}_{\rm Edd}$)	($L_{\rm Edd}$)	($L_{\rm Edd}$)	(km)
`D_d001`	0	(608, 512)	840	0.01	56	220	8.8	0.30	28.9
`DQ_d001`	1/3	(608, 512)	840	0.01	59	390	9.3	0.40	27.3
`QD_d001`	2/3	(608, 512)	840	0.01	55	310	21	0.47	21.2
`Q_d001`	1	(608, 512)	840	0.01	73	450	14	0.53	20.4
`D_d01`	0	(608, 512)	840	0.1	530	7800	86	43	16.3
`DQ_d01`	1/3	(608, 512)	840	0.1	410	10,000	77	34	11.2
`QD_d01`	2/3	(608, 512)	840	0.1	290	10,000	70	24	10.5
`Q_d01`	1	(608, 512)	840	0.1	390	11,000	76	25	10.3
`QD_d01_a`	2/3	(812, 512)	2100	0.1	370	6900	72	24	10.4
`Q_d01_a`	1	(812, 512)	2100	0.1	500	6800	81	26	10.4

Notes. The model names are shown in the first column: the capital letter "`D`" ("`Q`") means the dipole (quadrupole) magnetic field, and "`dXX`" denotes the maximum gas density of the initial torus. The ratio of the magnetic field strength $f = B_{\rm qua}/B_{\rm tot}$, the numerical grid points (N_r, N_θ), the radius of the outer boundary $r_{\rm out}$, the maximum gas density of the initial torus ρ_0, the mass accretion rate $\dot{M}_{\rm in}$, the mass outflow rate $\dot{M}_{\rm out}$, the radiative luminosity $L_{\rm rad}$, the kinetic luminosity $L_{\rm kin}$, and the magnetospheric radius $r_{\rm M}$ are presented.

$B_{\rm qua}$ are the dipole and quadrupole magnetic field strength at the NS's magnetic pole, respectively. Four cases of the magnetic field configuration of the NS parameterized by $f = B_{\rm qua}/B_{\rm tot} = 0$, 1/3, 2/3, and 1 are investigated. When $f = 0$ ($f = 1$), the NS has a pure dipole (quadrupole) magnetic field calculated from $A_\phi^{\rm dip}$ ($A_\phi^{\rm qua}$). Here, $A_\phi^{\rm dip}$ and $A_\phi^{\rm qua}$ are the vector potentials for the dipole and quadrupole magnetic fields, respectively (see Appendix in P. Das et al. 2022). In the cases of $f = 1/3$, 2/3, we calculate the NS's magnetic field from $A_\phi^{\rm dip} + A_\phi^{\rm qua}$ (M. Long et al. 2007). The direction of the quadrupole magnetic field is chosen so as to be parallel to that of the dipole one at $(r, \theta) = (r_{\rm NS}, 0)$. The computational domain consists of $[r_{\rm NS}, r_{\rm out}]$ and $[0, \pi]$, where $r_{\rm out}$ is the radius of the outer boundary. We run the simulations for $[0, 40{,}000 t_{\rm g}]$, where $t_{\rm g}$ is the light-crossing time for the gravitational radius of the NS, $r_{\rm g} = M_{\rm NS} = 2.1$ km. The size of the radial grid exponentially increases with r, while the grids in the θ-direction are uniformly distributed (H. R. Takahashi & K. Ohsuga 2017). Table 1 lists f for each model. In this table, the numerical grid points (N_r, N_θ), $r_{\rm out}$, the maximum gas density of the initial torus ρ_0, the mass accretion rate $\dot{M}_{\rm in}$, the mass outflow rate $\dot{M}_{\rm out}$, the radiative luminosity $L_{\rm rad}$, the kinetic luminosity $L_{\rm kin}$, and the magnetospheric radius $r_{\rm M}$ are also tabulated. Here, $\dot{M}_{\rm Edd} = L_{\rm Edd}$ is the Eddington mass accretion rate. The time-averaged values for $\dot{M}_{\rm in}$, $\dot{M}_{\rm out}$, $L_{\rm rad}$, $L_{\rm kin}$, and $r_{\rm M}$ are presented. The mass accretion rate and outflow rate are respectively obtained from

$$\dot{M}_{\rm in} = -\int_{r=r_{\rm NS}} \min[\rho u^r, 0]\sqrt{-g}\, d\theta d\phi, \tag{10}$$

$$\dot{M}_{\rm out} = \int_{r=r_{\rm out}} \max[\rho u^r, 0]\sqrt{-g}\, d\theta d\phi. \tag{11}$$

The radiative and kinetic luminosity are respectively calculated from (A. Sadowski et al. 2016)

$$L_{\rm rad} = -\int_{r=r_{\rm out}} \min[R^r_t, 0]\sqrt{-g}\, d\theta d\phi, \tag{12}$$

$$L_{\rm kin} = -\int_{r=r_{\rm out}} \min[\rho u^r(u_t + \sqrt{-g_{tt}}), 0]\sqrt{-g}\, d\theta d\phi. \tag{13}$$

In this study, $r_{\rm M}$ is defined as the maximum radius of the region, where the u_ϕ-weighted θ-average of $(p_{\rm gas} + p_{\rm rad})/p_{\rm mag}$ is smaller than unity (A. Inoue et al. 2023). Models `QD_d01_a` and `Q_d01_a` have the same initial parameters as models `QD_d01` and `Q_d01`, respectively, except for $r_{\rm out}$. These models are used to estimate the blackbody radius when the quadrupole magnetic field dominates in the magnetosphere (see Section 4 for detail).

We initially put a Fishbone and Moncrief torus (L. G. Fishbone & V. Moncrief 1976) as the source of the accreting gas. Under the condition of local thermodynamic equilibrium ($T_{\rm g} = T_{\rm r}$), we take $p_{\rm gas} + p_{\rm rad}$ inside the torus instead of $p_{\rm gas}$. We set the radius of the torus inner edge to 210 km and the maximum pressure radius to 304.5 km. In addition to the dipole and quadrupole magnetic fields of the NS, the poloidal-loop magnetic fields whose vector potential is proportional to $\max(\rho/\rho_0 - 0.2, 0)$ are put inside the torus. The embedded loop magnetic fields are antiparallel to the dipole magnetic field at the torus inner edge (M. M. Romanova et al. 2011; K. Parfrey & A. Tchekhovskoy 2017; H. R. Takahashi & K. Ohsuga 2017). On the other hand, for $r < 304.5$ km, the initial loop magnetic fields are antiparallel to quadrupole magnetic fields in the upper hemisphere and parallel to them in the lower hemisphere at the torus surface. We impose $\max[p_{\rm gas} + p_{\rm rad}]/\max[p_{\rm mag}] = 100$ on the loop magnetic field and impose a perturbation on $p_{\rm gas} + p_{\rm rad}$ of 10% to break an equilibrium state. The NS and torus are surrounded by the relatively hot and low-density corona with a density of $\rho_{\rm col}$ and pressure of $p_{\rm col}$ (see Section 2.2 of A. Inoue et al. 2023). The gas velocity of the corona is $u^i = u^i_{\rm col} = 0$. We set the outflowing boundary at $r = r_{\rm out}$ and the reflective boundary at $\theta = 0$, π. At $r = r_{\rm NS}$, the gas is swallowed by the NS, but the energy is not swallowed by the NS (K. Ohsuga 2007; A. Inoue et al. 2023).

We adopt the simplified version of the method proposed by K. Parfrey & A. Tchekhovskoy (2017, 2023) to solve the GR-RMHD equations stably. The concept of their prescription is to divide the fluid into the contributions from the GR-MHD flows and from the numerical floor. To do so, we solve $\nabla_\mu(\mathcal{F}\rho u^\mu) = 0$ in addition to Equations (1)–(4). Here, $\mathcal{F}$ is evolved as a passive scalar. We initialize $\mathcal{F} = 1$ inside the torus while $\mathcal{F} = 0$ outside the torus. Using $\mathcal{F}$, we adjust the fluid quantities $q = (\rho, p_{\rm gas}, u^i)$. In the region of $\mathcal{F} = 0$, we replace q with the quantities of the initial corona $q_{\rm col} = (\rho_{\rm col}, p_{\rm col}, u^i_{\rm col})$. On the other hand, q is not modified in the region of $\mathcal{F} = 1$. When $0 < \mathcal{F} < 1$, the fluid

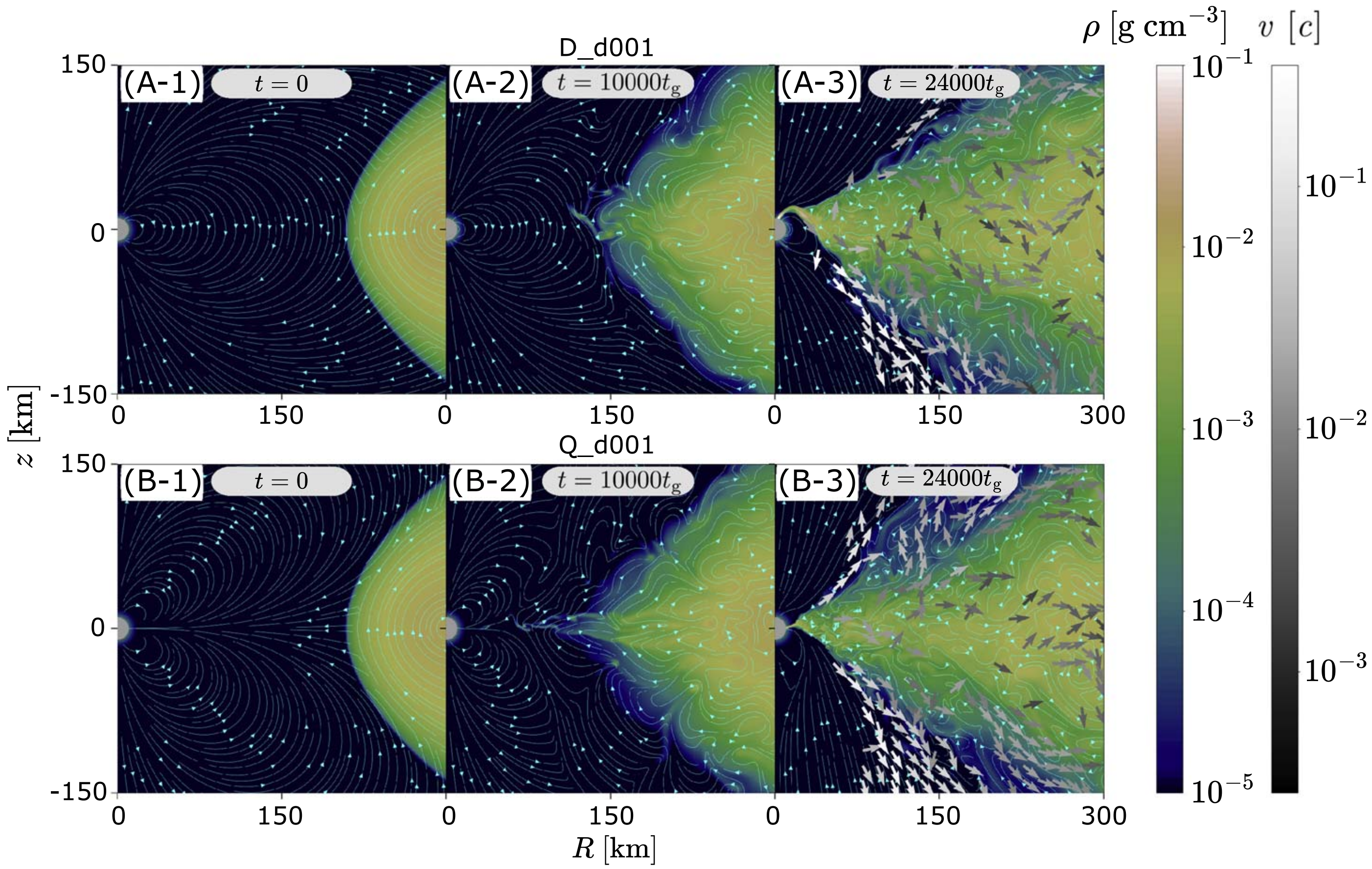

Figure 1. Gas density distribution at $t=0$, 10,000t_g, 24,000t_g for models `D_d001` and `Q_d001`. Stream plots are magnetic field vectors. Vectors in panels (A-3) and (B-3) are the gas velocity vectors in the region where $4\pi r^2 \rho u^r > \dot{M}_{\rm Edd}$. Here, the color of each vector indicates the magnitude of the velocity in the poloidal direction. The gray region of $r < 10$km is the NS.

quantities are linearly interpolated with weight $\mathcal{F}$ between q_* and $q_{\rm col}$ as $q = q_{\rm col} + (q_* - q_{\rm col})\mathcal{F}$. Here, $q_* = (\rho_*, p_*, u_*^i)$ are the gas density (ρ_*), pressure (p_*), and velocity (u_*^i) calculated from the conservative variables. We take $\kappa_{\rm sca} = 0$ and $\kappa_{\rm abs} = 0$ in the regions where $\mathcal{F} < 0.9$ and $\sigma = b^2/\rho > 10$, for numerical stability.

3. Result

3.1. Accretion Structure

In Figure 1, we describe the time evolution of the gas density distribution and the magnetic field. Here, $(R, z) = (r\sin\theta, r\cos\theta)$. We present the results of models `D_d001` (upper panels) and `Q_d001` (lower panels). The NS is depicted by the gray region of $r < 10$km, and its center is located at the origin $(R, z) = (0, 0)$. Stream plots represent the magnetic field vectors. Vectors in panels (A-3) and (B-3) are the gas velocity vectors in the poloidal direction, which are plotted only in the region where $4\pi r^2 \rho u^r > \dot{M}_{\rm Edd}$. The color of each vector indicates the magnitude of the velocity in the poloidal direction. As mentioned in Section 2, the dipole magnetic field is antiparallel to the loop magnetic field at the inner edge of the torus (see panel (A-1)). On the other hand, the quadrupole magnetic field is antiparallel (parallel) to the loop magnetic field at the torus surface in the upper (lower) hemisphere (see panel (B-1)).

After the onset of the simulations, the system starts to deviate from the equilibrium state. The gas goes inward due to the Maxwell stress induced by the magnetorotational instability (MRI; S. A. Balbus & J. F. Hawley 1991) (panels (A-2) and (B-2)). The embedded loop magnetic fields reconnect with the initially closed magnetic fields of the NS, causing the NS's magnetic field lines to open up. The accretion disk is formed near the equatorial plane, $z = 0$ (see panels (A-3) and (B-3)).

As can be seen from the velocity vectors, outflows emanate from the accretion disk. Such outflows are driven by the radiation force and centrifugal force, and they appear in all models. Although not shown in this figure, the effective optical depth of the outflows measured from the outer boundary in the r-direction exceeds unity (T. Ogawa et al. 2017; A. Inoue et al. 2023). This implies that the outflows from the super-Eddington accretion disk produce thermal emission, regardless of whether the NS's magnetic field is a dipole or quadrupole. Furthermore, when estimated using the same method as A. Inoue et al. (2023), the blackbody radii are consistent with the relation of $r_{\rm bb} = 3.2(\dot{M}_{\rm in}/\dot{M}_{\rm Edd})^{0.71}$ in A. Inoue et al. (2023), even if the quadrupole magnetic field dominates inside the magnetosphere (51 km in model `Q_d001`, 170 km in model `QD_d01_a`, and 160 km in model `Q_d01_a`). The magnitude of the poloidal velocity in the regions around $\theta \sim 45^\circ$ and 135° is larger than that in the range of $45^\circ \lesssim \theta \lesssim 135^\circ$ and exceeds $0.1c$. Since the gas density in these regions is very low, the radiation from the accretion flows effectively accelerates the outflowing gas (K. Ohsuga & S. Mineshige 2007).

The accretion flows along the dipole or quadrupole magnetic field lines exist near the NS. The details of these structures will

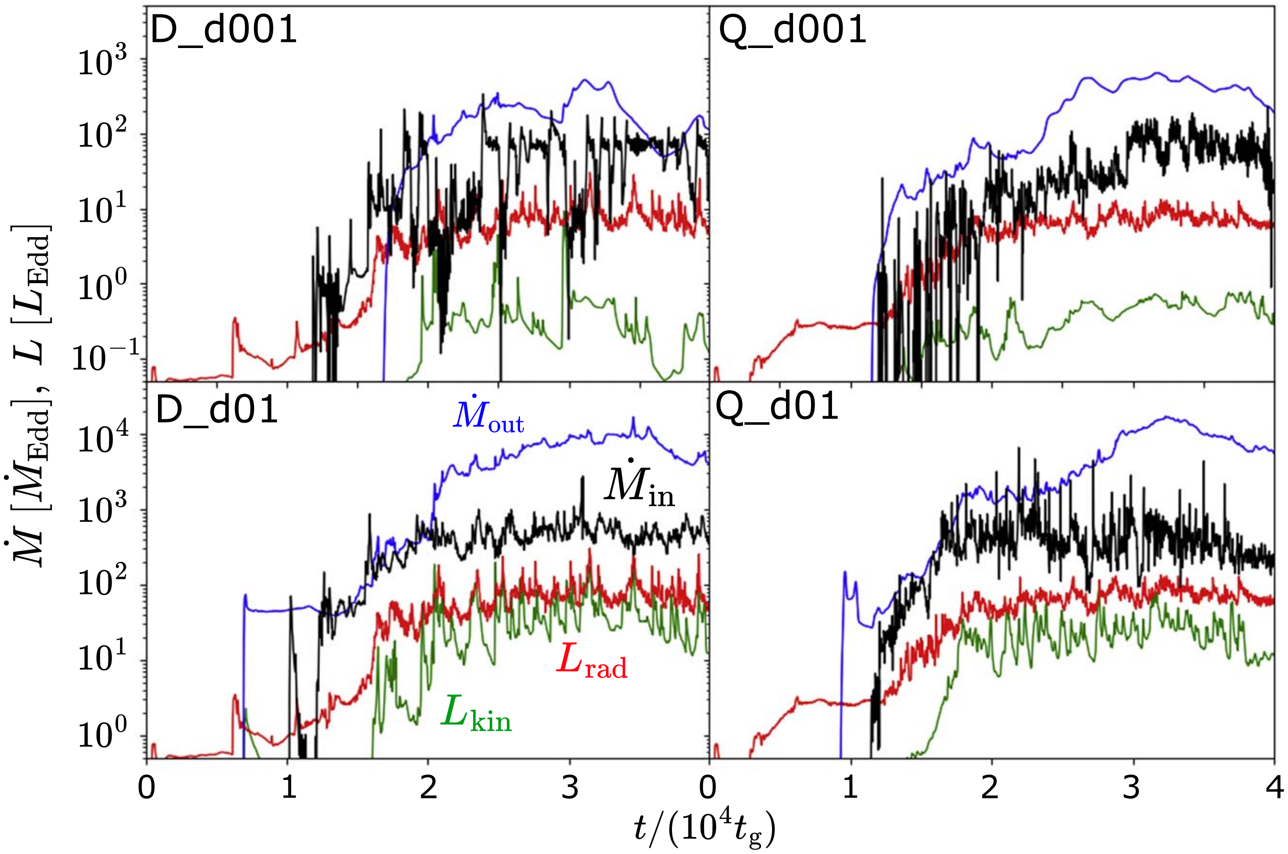

Figure 2. Time evolution of the mass accretion rate (black), outflow rate (blue), radiative luminosity (red), and kinetic luminosity (green).

be explained later. In models of $\rho_0 = 0.01$ g cm^{-3}, the radiative shock arises above the NS surface (see Appendix A for details). On the other hand, such a structure cannot be seen in models of $\rho_0 = 0.1$ g cm^{-3}. The past numerical simulations carefully examined the radiative shock structure (T. Kawashima et al. 2016; T. Kawashima & K. Ohsuga 2020; L. Zhang et al. 2022, 2023; P. Abolmasov & G. Lipunova 2023), but the detailed structure is out of the scope of this study.

We should stress here that the super-Eddington accretion is feasible since a large amount of the radiation energy escapes from the side wall of the accretion column (see Appendix B), which has been shown by T. Kawashima et al. (2016). It reduces the radiation energy density inside the column ($\hat{E} = u_\mu u_\nu R^{\mu\nu}$), leading to a reduction of the outward radiation flux in the fluid frame, $\hat{F}_{\rm rad} \sim (c/\tau)\hat{E}$. The resulting order of $\kappa_{\rm es}\hat{F}_{\rm rad}/g$ ($g = M_{\rm NS}/r^2$) inside the column is unity (see also T. Kawashima et al. 2016), which reduces the gas infall velocity but is not sufficient to prevent the gas accretion. Thus, super-Eddington accretion onto the magnetized NS through the accretion columns is feasible.

We plot $\dot{M}_{\rm in}$, $\dot{M}_{\rm out}$, $L_{\rm rad}$, and $L_{\rm kin}$ as a function of time in Figure 2. Here, the results of models `D_d001`, `Q_d001`, `D_d01`, and `Q_d01` are presented. It can be seen that $\dot{M}_{\rm in}$, $\dot{M}_{\rm out}$, $L_{\rm rad}$, and $L_{\rm kin}$ gradually increase after the simulations start, and these quantities are in the quasi-steady state for [30,000$t_{\rm g}$, 40,000$t_{\rm g}$]. Such time evolution profiles are true for the $\dot{M}_{\rm in}$, $\dot{M}_{\rm out}$, $L_{\rm rad}$, and $L_{\rm kin}$ of the other models. Therefore, we hereafter show the time-averaged results in [30,000$t_{\rm g}$, 40,000$t_{\rm g}$]. In this time interval, the inflow–outflow structures in all models are in a quasi-steady state within $r \sim 100$ km (i.e., the net flow rate $\dot{M}_{\rm in} - \dot{M}_{\rm out}$ is almost constant within $r \sim 100$ km).

We find that $\dot{M}_{\rm in}$, $\dot{M}_{\rm out}$, $L_{\rm rad}$, and $L_{\rm kin}$ in models of $\rho_0 = 0.1$ g cm^{-3} are larger than those in models of $\rho_0 = 0.01$ g cm^{-3} (see also Table 1). On the other hand, we cannot find any clear dependence of $\dot{M}_{\rm in}$, $\dot{M}_{\rm out}$, $L_{\rm rad}$, and $L_{\rm kin}$ on f. We can also see that $\dot{M}_{\rm out}$ in models `QD_d01` and `Q_d01` is slightly greater than in models `QD_d01_a` and `Q_d01_a`. This difference arises from the small $r_{\rm out}$ in models `QD_d01` and `Q_d01`. In these models, the radial gas velocity for $45° \lesssim \theta \lesssim 135°$ is smaller than the escape velocity, even at $r_{\rm out} = 840$ km. Although a fraction of such gases do not reach $r = 2100$ km, all gas at $r_{\rm out}$ is included in the integration of Equation (11). This leads to a larger $\dot{M}_{\rm out}$ in models `QD_d01` and `Q_d01` compared to that in models `QD_d01_a` and `Q_d01_a`.

Figure 3 shows $L_{\rm kin}/L_{\rm rad}$ as a function of f. We can see that the $L_{\rm kin}/L_{\rm rad}$ in models of $\rho_0 = 0.1$ g cm^{-3} is about 10 times greater than that in models of $\rho_0 = 0.01$ g cm^{-3}. This trend has also been reported in past numerical simulations (K. Ohsuga 2007; A. Inoue et al. 2023). We cannot find the dependence of $L_{\rm kin}/L_{\rm rad}$ on f.

Next, we explain that the accretion flows along the dipole (quadrupole) magnetic field lines are formed near the NS surface when the dipole (quadrupole) magnetic fields are dominant at $r_{\rm M}$. Figure 4 illustrates the time-averaged gas density (color) and magnetic field lines (cyan solid lines). In models `D_d001`, `DQ_d001`, `QD_d001`, `D_d01`, and `DQ_d01`, the accretion flows roughly follow the dipole magnetic field lines (we refer to such accretion flows as dipolar accretion flows). The accretion disk is truncated by the NS's magnetic field, and accretion columns are formed near the magnetic poles

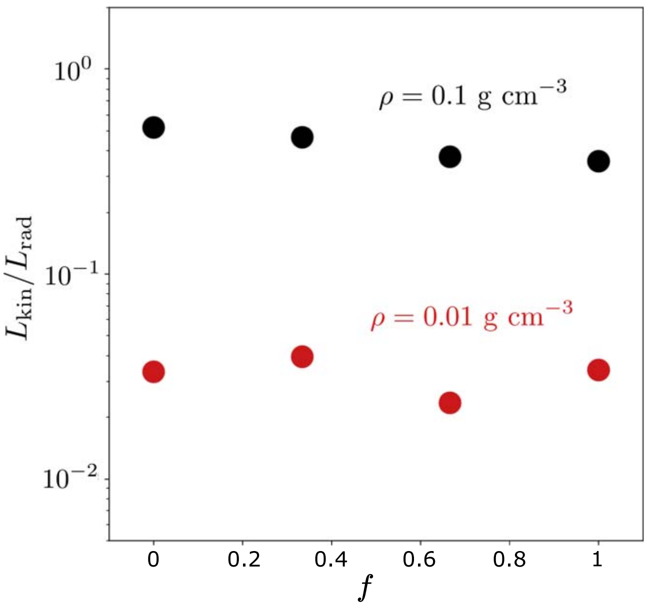

Figure 3. The ratio of the kinetic luminosity to the radiative luminosity as a function of *f*.

of the NS, at $(R, z) \sim$ (4 km, 11 km) for model D_d001, at $(R, z) \sim$ (6 km, −11 km) for model DQ_d001, at $(R, z) \sim$ (11 km, −5 km) for model QD_d001, at $(R, z) \sim$ (6 km, ±10 km) for model D_d01, and at $(R, z) \sim$ (7 km, 10 km) and ∼(9 km, −8 km) for model DQ_d01. When we define the truncation radius as the radius at which $\sigma = 1$ on the equatorial plane, the truncation radius coincides with the magnetospheric radius $r_{\rm M}$ within a factor of two.

In models Q_d001, QD_d01, and Q_d01, the accretion flows along the quadrupole magnetic field lines can be seen. We name such accretion flows quadrupolar accretion flows. In these models, $p_{\rm dip}(r_{\rm M}) < p_{\rm qua}(r_{\rm M})$ holds ($p_{\rm dip}/p_{\rm qua} \sim 0.26$ for model QD_d001). Here, $p_{\rm dip} = B_{\rm dip}^2/(8\pi)(r_{\rm NS}/r)^6$ and $p_{\rm qua} = B_{\rm qua}^2/(8\pi)(r_{\rm NS}/r)^8$ represent the magnetic pressure originating from the dipole and quadrupole magnetic field, respectively. The high-density region existing around the equatorial plane within $r_{\rm M}$ is an accretion belt (M. Long et al. 2007; P. Das et al. 2022). As illustrated in Figure 4, such an accretion belt appears at $(R, z) \sim$ (12 km, 1 km) for model Q_d001, at $(R, z) \sim$ (10 km, 0 km) for model QD_d01, and at $(R, z) \sim$ (10 km, 2 km) for model Q_d01. The angular momentum of the accreting gas within $r_{\rm M}$ is about one-tenth of the Keplerian angular momentum. The accretion belt has lost angular momentum due to the quadrupole magnetic field and exhibits different properties compared to the accretion disk outside the magnetospheric radius (see Section 3.2). In the quadrupolar accretion flow models with relatively high rates of mass accretion (QD_d01 and Q_d01), the accretion column is also formed at $(R, z) \sim$ (7 km, 10 km). The accreting matter does not reach the NS surface in the lower hemisphere in models Q_d001, QD_d01, and Q_d01. The reason for this is that the open magnetic field lines reaching the outer boundary in the lower hemisphere prevent the gas from falling onto the lower hemisphere of the NS (see also P. Das et al. 2022).

For a fixed $\dot{M}_{\rm in}$, the magnetospheric radius $r_{\rm M}$ tends to be small for the models with a large *f* (see Table 1). The reason for this is that $p_{\rm qua}(r)$ decreases with distance from the NS more rapidly than $p_{\rm dip}(r)$. The magnetospheric radius in models of $\rho_0 = 0.1$ g cm^{-3} is smaller than that in models of $\rho_0 = 0.01$ g cm^{-3}. This is because, the larger the mass accretion rate, the larger the radiation pressure, which leads to a smaller $r_{\rm M}$ for a fixed magnetic pressure.

When the gas in the disk reaches at $R = r_{\rm M}$, it moves along the last closed field line toward the lower gravitational potential. As a result, a single accretion stream is formed in models of $\rho_0 = 0.01$ g cm^{-3} (upper panels).[5] On the other hand, in models with $\rho_0 = 0.1$ g cm^{-3}, $R = r_{\rm M}$ is close to NS and the disk is geometrically thick, such that two flows moving toward the direction of low gravitational potential appear along the last closed field line (dual accretion stream) as shown in the lower panels.

The photospheres for scattering and effective absorption, which are integrated from the rotational axis, are shown by yellow and magenta lines, respectively. Here, we define total ($\tau_{\rm tot}$) and effective optical depth ($\tau_{\rm eff}$) as follows:

$$\tau_{\rm tot} = \int \rho(\kappa_{\rm abs} + \kappa_{\rm es})\sqrt{g_{\theta\theta}}\,d\theta, \tag{14}$$

$$\tau_{\rm eff} = \int \rho\sqrt{(\kappa_{\rm abs} + \kappa_{\rm es})\kappa_{\rm abs}}\sqrt{g_{\theta\theta}}\,d\theta. \tag{15}$$

In models with $\rho_0 = 0.01$ g cm^{-3}, the larger *f*, the larger $r_{\rm eff}^{\rm min}$. Here, $r_{\rm eff}^{\rm min}$ is the minimum *r* for the region with $\tau_{\rm eff} > 1$ (the region enclosed by the magenta line). For instance, $r_{\rm eff}^{\rm min} \sim 20$ km for model D_d001, while $r_{\rm eff}^{\rm min} \sim 40$ km for model Q_d001. This tendency arises from the fact that the disk gas density decreases as *f* increases. In model D_d001, the relatively high-density disk exists because the accreting gas accumulates around $r = r_{\rm M}$ near the equatorial plane, due to the magnetic pressure originating from the dipole magnetic field. This leads to the large $\kappa_{\rm abs}$, resulting in the small $r_{\rm eff}^{\rm min}$. Actually, although the mass accretion rate at $r = 40$ km is $\sim 100\,\dot{M}_{\rm Edd}$ in both models, $(v^{(r)}, \Sigma) \sim (10^{-3}c, 10^4$ g cm$^{-2})$ for model D_d001 and $(v^{(r)}, \Sigma) \sim (10^{-2}c, 10^3$ g cm$^{-2})$ for model Q_d001. Here, $v^{(r)} = u^{(r)}/u^{(t)}$ is the radial gas velocity, where the parentheses denote the quantities in the static observer frame, and $\Sigma = \int_0^\pi \rho\sqrt{g_{\theta\theta}}\,d\theta$ is the surface gas density. It is also obvious that the values of $r_{\rm eff}^{\rm min}$ for models DQ_d001 and QD_d001 are larger (smaller) than that for model D_d001 (Q_d001). In models of $\rho_0 = 0.1$ g cm^{-3}, the gas density is high enough for $r_{\rm eff}^{\rm min} = r_{\rm NS}$.

The opening angle of the photosphere for scattering in models of $\rho_0 = 0.1$ g cm^{-3} is smaller than in models of $\rho_0 = 0.01$ g cm^{-3}. This is because the gas density of the outflows gets larger as the mass accretion rate increases. In all models, we expect that the observed radiation spectra are affected by Comptonization, since the total optical depth $\tau_{\rm tot}$ at the effective photosphere highly exceeds 100. The gas temperature weighted by $\Delta\tau_{\rm es} = \rho\kappa_{\rm es}\sqrt{g_{\theta\theta}}\Delta\theta$ is averaged

---

[5] In the case of model D_d001, despite the NS having only a dipole magnetic field, gas falls onto only one of the poles. The reason is as follows. As the gas from the torus reaches the magnetosphere, it accretes toward one of the poles, and which pole the gas falls onto is determined by the embedded perturbation in the torus. Then, the ram pressure of the gas distorts the last closed field line and tilts it with respect to the equatorial plane (see the last closed magnetic field line depicted in the panel of D_d001). As the magnetic field lines tilt, the subsequent gas tends to flow in the direction in which the preceding gas accreted. Thus, an accretion column forms on the side where the gas first accretes.

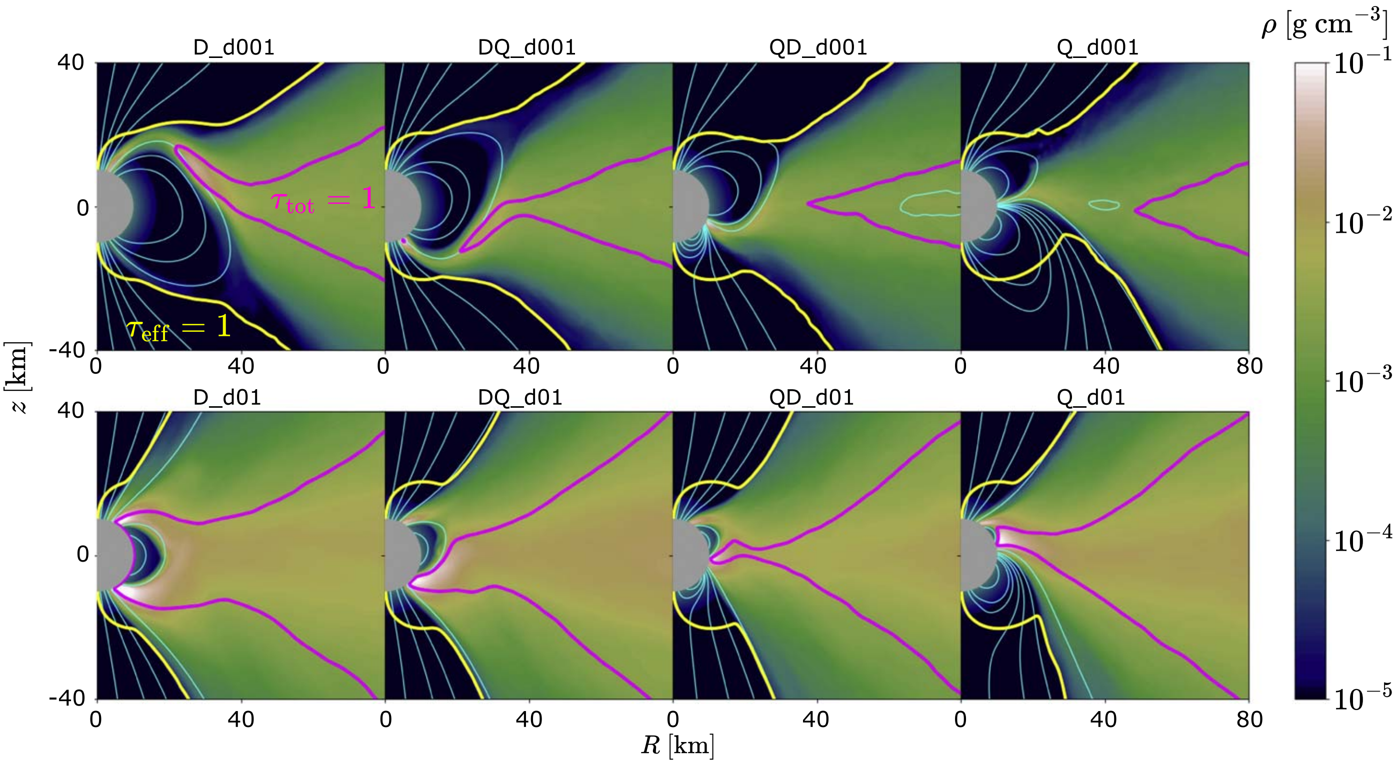

Figure 4. Time-averaged gas density map with magnetic field lines (cyan solid lines). Yellow lines and magenta lines represent the photosphere for the total optical depth and effective absorption, respectively.

over θ within the region where $\tau_{\rm tot} > 1$ and $\tau_{\rm eff} < 1$, resulting in $\sim 10^7$ K. This leads to the Compton y-parameter $y = (4kT_{\rm e}/mc^2)\tau_{\rm tot}^2$ being larger than unity (see Section 4 for details).

In Figure 5, the polar angle of the accretion flows at the NS surface $\theta_{\rm peak}$ as a function of f is shown. Here, $\theta_{\rm peak}$ is defined as the polar angle where $-2\pi r^2 \rho u^r \sin\theta$ is maximum in each region of $0° < \theta < 60°$ and $60° < \theta < 180°$. The accretion flow formed in the region of $\mathcal{F} < 0.9$ or $\sigma > 10$ is ignored where we artificially reduce the emission and absorption processed for numerical stability. The marker size is proportional to the mass accretion rate at the NS surface integrated within $\theta_{\rm peak} - 15° < \theta < \theta_{\rm peak} + 15°$,

$$\dot{M}_{\rm in}^{\rm upper(lower)} = -2\pi \int_{\theta_{\rm peak}-15^\circ}^{\theta_{\rm peak}+15^\circ} \min[\rho u^r, 0]\sqrt{-g}\, d\theta, \tag{16}$$

where the mass accretion rate of the accretion flow closer to $\theta = 0°$ (180°) is denoted by "upper" ("lower"). Table 2 lists $\dot{M}_{\rm in}^{\rm upper}$ and $\dot{M}_{\rm in}^{\rm lower}$. In this table, $L_{\rm rad}^{\rm upper}$ and $L_{\rm rad}^{\rm lower}$ are also presented. Here, $L_{\rm rad}^{\rm upper}$ ($L_{\rm rad}^{\rm lower}$) is the radiative luminosity obtained by integrating over the spherical surface of the upper (lower) hemispheres at $r = r_{\rm out}$. The single accretion stream is formed when $\rho_0 = 0.01$ g cm^{-3}. Therefore, there is one point (red point) for a given f, and $\dot{M}_{\rm in}^{\rm lower}$ cannot be defined. On the other hand, in the case of $\rho_0 = 0.1$ g cm^{-3}, dual accretion streams appear, so two points (black points) are plotted for a given f. The polar angle of the high-density region near the NS surface illustrated in Figure 4 is consistent with $\theta_{\rm peak}$. In models of $\rho_0 = 0.01$ g cm^{-3}, $\theta_{\rm peak}$ approaches 90° as f increases. To give a specific example, $\theta_{\rm peak} \sim 30°$ for model `D_d001`, and $\theta_{\rm peak} \sim 90°$ for model `Q_d001`. When $\rho_0 = 0.1$ g cm^{-3}, the $\theta_{\rm peak}$ closer to $\theta = 180°$ decreases as f increases. Actually, the $\theta_{\rm peak}$ closer to $\theta = 180°$ is $\sim 150°$ for model `D_d01` and $\sim 70°$ for model `Q_d01`. In these models, the $\theta_{\rm peak}$ closer to $\theta = 0°$ is $\theta_{\rm peak} \sim 30°$ and does not so depend on f.

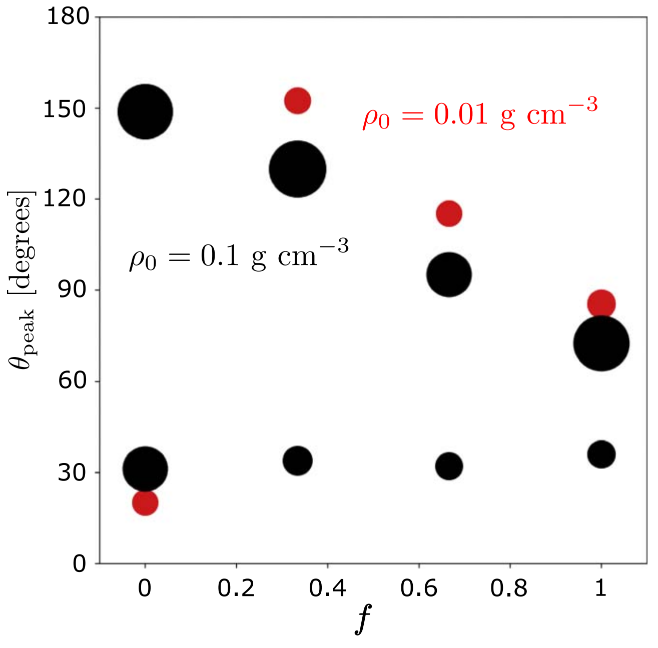

Figure 5. The position angle ($\theta_{\rm peak}$) of the accretion column and belt as a function of f. Here, we define $\theta_{\rm peak}$ as the polar angle at which $-2\pi r^2 \rho u^r$ is maximum in each region of $0° < \theta < 60°$ and $60° < \theta < 180°$. The marker size is proportional to the mass accretion rate of the column or belt $\dot{M}_{\rm in}^{\rm upper(lower)}$ (see Equation 16). The magnetic pole on the upper (lower) hemisphere corresponds to 0° (180°), and 90° represents the equatorial plane.

Table 2
The Accretion Rate and Radiative Luminosity

Model	$\dot{M}_{\rm in}^{\rm upper}$ $[\dot{M}_{\rm Edd}]$	$\dot{M}_{\rm in}^{\rm lower}$ $[\dot{M}_{\rm Edd}]$	$L_{\rm rad}^{\rm upper}$ $[L_{\rm Edd}]$	$L_{\rm rad}^{\rm lower}$ $[L_{\rm Edd}]$
`D_d001`	20	⋯	2.4	5.9
`DQ_d001`	58	⋯	5.3	3.6
`QD_d001`	55	⋯	6.7	13
`Q_d001`	73	⋯	7.5	6.3
`D_d01`	220	310	48	34
`DQ_d01`	84	330	43	29
`QD_d01`	68	220	36	29
`Q_d01`	71	310	33	37

When comparing models of the same f with each other, $\theta_{\rm peak}$ for the model of $\rho_0 = 0.01\,{\rm g\,cm^{-3}}$ is either greater than the larger $\theta_{\rm peak}$ or less than the smaller $\theta_{\rm peak}$ for the model of $\rho_0 = 0.1\,{\rm g\,cm^{-3}}$. This arises from the fact that the magnetospheric radius in the models with a low rate of mass accretion is larger than that in the models with a high rate of mass accretion. As the magnetospheric radius increases, the last closed magnetic field line connects the polar angle closer to the NS's magnetic pole. This results in gas accreting at an angle nearer to the magnetic poles. The result that $\theta_{\rm peak}$ depends on both f and ρ_0 implies that the angular distribution of the radiation flux near the NS is also dependent on both f and ρ_0. This point will be explained in Section 3.3.

Since the gas density distribution in model `D_d01` is approximately symmetric with respect to the equator, $\dot{M}_{\rm in}^{\rm upper}$ is comparable to $\dot{M}_{\rm in}^{\rm lower}$. On the other hand, $\dot{M}_{\rm in}^{\rm lower} \sim (3\ {\rm to}\ -4)\dot{M}_{\rm in}^{\rm upper}$ in models `DQ_d01`, `QD_d01`, and `Q_d01`. This is because the NS's magnetic field deviates from the dipole field, due to the quadrupole component making it easier for gas to accrete mainly in the region of $60° < \theta < 180°$. Despite the asymmetric accretion flows with respect to the equatorial plane in models `D_d001`, `DQ_d001`, `QD_d001`, `DQ_d01`, `QD_d01`, and `Q_d01`, $L_{\rm rad}^{\rm upper} \sim L_{\rm rad}^{\rm lower}$ holds in all models, and the difference between $L_{\rm rad}^{\rm upper}$ and $L_{\rm rad}^{\rm lower}$ is at most a factor of two. The reason for this will be presented in Section 3.3.

3.2. Angular Momentum Transfer

Next, we demonstrate that the angular momentum of the accreting gas is transported to the NS via the dipole or quadrupole fields. Figure 6 displays the distribution of the angular momentum flux for models `D_d001` ($r_{\rm M} \sim 29$ km) and `Q_d001` ($r_{\rm M} \sim 20$ km). The red region represents the inward (negative) angular momentum flux, while the outward (positive) angular momentum flux is illustrated in the blue region. Black vectors in panels (a), (c) and (b), (d) are the vectors of $({T_{\rm MA}}_{\phi}^{(r)}, {T_{\rm MA}}_{\phi}^{(\theta)})$ and $({T_{\rm EM}}_{\phi}^{(r)}, {T_{\rm EM}}_{\phi}^{(\theta)})$, respectively. In model `D_d001`, ${T_{\rm MA}}_{\phi}^{r}$ is negative inside the disk region, which indicates that the angular momentum is transported inward due to the gas accretion (see panel (a)). It can also be seen that the $|{T_{\rm MA}}_{\phi}^{r}|$ for $R \lesssim r_{\rm M}$ is smaller than the $|{T_{\rm MA}}_{\phi}^{r}|$ for $R \gtrsim r_{\rm M}$. The reason for the decrease in $|{T_{\rm MA}}_{\phi}^{r}|$ is that the inward ${T_{\rm MA}}_{\phi}^{r}$ is converted into the inward ${T_{\rm EM}}_{\phi}^{r}$ at $R \sim r_{\rm M}$ via the interaction between the dipole magnetic field and the accreting matter. Actually, the inward ${T_{\rm EM}}_{\phi}^{r}$ appears for $R \lesssim r_{\rm M}$, and the black vectors point from $(R, z) \sim (r_{\rm M}, 0)$ to $(R, z) \sim (5\,{\rm km}, \pm 8\,{\rm km})$ (see panel (b)). This inward ${T_{\rm EM}}_{\phi}^{r}$ leads the NS to spin up. Although the mass accretion rate at the NS surface in the lower hemisphere is small, the inward angular momentum flux is significant near both magnetic poles. In fact, $2\pi {T_{\rm EM}}_{\phi}^{r}\sqrt{-g} \sim 5 \times 10^{36}\,{\rm g\,cm^2\,s^{-2}}$ at $(R, z) \sim (5\,{\rm km}, 8\,{\rm km})$, and $2\pi {T_{\rm EM}}_{\phi}^{r}\sqrt{-g} \sim 2 \times 10^{36}\,{\rm g\,cm^2\,s^{-2}}$ at $(R, z) \sim (5\,{\rm km}, -8\,{\rm km})$. Since the upper and lower hemispheres of the NS connect each other by magnetic field lines, the angular momentum transferred by the gas accretion around $R \sim r_{\rm M}$ is conveyed to both hemispheres through the magnetic field.

In model `Q_d001` as well, the angular momentum of the accreting gas is transferred to the NS via the quadrupole magnetic field. We find that ${T_{\rm MA}}_{\phi}^{r}$ is negative in the disk region, but its absolute value decreases at around $(R, z) = (10\,{\rm km}, 0)$, where it is replaced by a significant inward ${T_{\rm EM}}_{\phi}^{r}$ (see panel (d)). In addition, the angular momentum is also transferred to NS around $(R, z) \sim (5\,{\rm km}, 8\,{\rm km})$, where the mass accretion rate is low. This structure is similar to the lower hemisphere in model `D_d001`. The angular momentum transport can happen even outside accretion columns and accretion belts. In the disk region for both models `D_d001` and `Q_d001`, ${T_{\rm EM}}_{\phi}^{r}$ is positive. In this region, the angular momentum is transported outward due to the MRI turbulence, which enables the disk gas to accrete. Although not shown in this figure, in all models, the radiation angular momentum flux R_{ϕ}^{r} contributes little to the NS's spin-up. The reason for this is that $u^{\mu} \sim u_{\rm R}^{\mu}$ and $\rho \gg \bar{E}$ hold inside the super-Eddington accretion disk. These relations lead to ${T_{\rm MA}}_{\phi}^{r}/R_{\phi}^{r} \sim \rho/\bar{E} \gg 1$ at $R \sim r_{\rm M}$.

It is also evident from Figure 7 that the spin-up of the NS is primarily induced by the angular momentum flux of the electromagnetic field. We plot the angular momentum fluxes of the electromagnetic field $\dot{L}_{\rm EM}$ (blue plots), of the accreting matter $\dot{L}_{\rm MA}$ (gray plots), and of the radiation $\dot{L}_{\rm RA}$ (red plots) normalized by $\dot{M}_{\rm in}$. They are defined as

$$\dot{L}_{\rm MA} = -2\pi \int {T_{\rm MA}}_{\phi}^{r}\sqrt{-g}\,d\theta, \tag{17}$$

$$\dot{L}_{\rm EM} = -2\pi \int {T_{\rm EM}}_{\phi}^{r}\sqrt{-g}\,d\theta, \tag{18}$$

$$\dot{L}_{\rm RA} = -2\pi \int R_{\phi}^{r}\sqrt{-g}\,d\theta. \tag{19}$$

In all models, $\dot{L}_{\rm EM}/\dot{M}_{\rm in}$ is dominant over the other fluxes.

Due to the conversion of gas angular momentum into that of the electromagnetic field near $r \sim r_{\rm M}$, the specific angular momentum of the gas there approximately coincides with $\dot{L}_{\rm EM}/\dot{M}_{\rm in}$. The specific angular momentum at $r = r_{\rm M}$ is analytically evaluated as

$$l_{\rm dip} = 1.9 \times 10^{16}[{\rm cm^2\,s^{-1}}]\left(\frac{\alpha}{0.1}\right)^{1/7} \times \left(\frac{\dot{M}_{\rm in}}{100\dot{M}_{\rm Edd}}\right)^{-1/7}\left(\frac{B_{\rm dip}}{10^{10}\,{\rm G}}\right)^{2/7}\left(\frac{M_{\rm NS}}{1.4M_{\odot}}\right)^{2/7}\left(\frac{r_{\rm NS}}{10\ \ {\rm km}}\right)^{6/7} \tag{20}$$

for $f = 0$ and

$$l_{\rm qua} = 1.7 \times 10^{16}[{\rm cm^2\,s^{-1}}]\left(\frac{\alpha}{0.1}\right)^{1/11}\left(\frac{\dot{M}_{\rm in}}{100\dot{M}_{\rm Edd}}\right)^{-1/11} \times \left(\frac{B_{\rm qua}}{10^{10}\,{\rm G}}\right)^{2/11}\left(\frac{M_{\rm NS}}{1.4M_{\odot}}\right)^{4/11}\left(\frac{r_{\rm NS}}{10\ \ {\rm km}}\right)^{8/11} \tag{21}$$

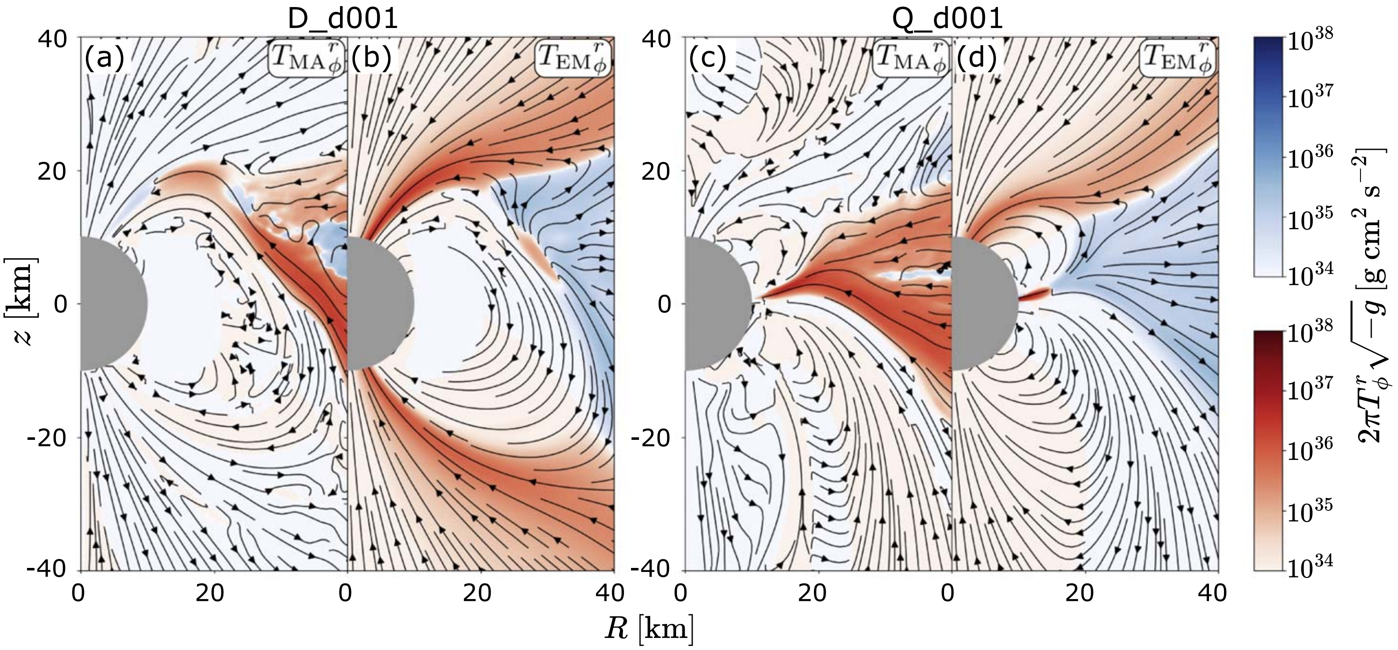

Figure 6. Color contour plots of the angular momentum flux. The red (blue) region represents the negative (positive) angular momentum flux. Black vectors depict the poloidal components of the angular momentum flux.

for $f = 1$, by calculating $r_{\rm M}$ from the balance between the radiation pressure of the self-similar solution of the slim disk (K.-y. Watarai & J. Fukue 1999) and the magnetic pressure arising from the NS's magnetic field (H. R. Takahashi & K. Ohsuga 2017). Here, α denotes the viscous parameter. By applying $\alpha = 0.1$, $M_{\rm NS} = 1.4\,M_{\odot}$, and $r_{\rm NS} = 10$ km, we obtain $l_{\rm dip} \sim 2.2 \times 10^{16}\,{\rm cm^2\,s^{-1}}$ ($\sim 3.1 \times 10^{16}\,{\rm cm^2\,s^{-1}}$) for model `D_d01`(`D_d001`), because $B_{\rm dip} = 4 \times 10^{10}$ G and $\dot{M}_{\rm in} = 530\dot{M}_{\rm Edd}$ ($56\,\dot{M}_{\rm Edd}$). Similarly, by setting $B_{\rm qua} = 4 \times 10^{10}$ G and $\dot{M}_{\rm in} = 390\,\dot{M}_{\rm Edd}$ ($73\dot{M}_{\rm Edd}$), the $l_{\rm qua}$ of model `Q_d01`(model `Q_d001`) is calculated as $\sim 2.1 \times 10^{16}\,{\rm cm^2\,s^{-1}}$($\sim 2.2 \times 10^{16}\,{\rm cm^2\,s^{-1}}$). These $l_{\rm dip}$ and $l_{\rm qua}$ are consistent with the $\dot{L}_{\rm EM}/\dot{M}_{\rm in}$ obtained by the present simulations. The value of $\dot{L}_{\rm EM}/\dot{M}_{\rm in}$ is higher in the models with $\rho_0 = 0.01\,{\rm g\,cm^{-3}}$ than in the models with $\rho_0 = 0.01\,{\rm g\,cm^{-3}}$due to the lower mass accretion rate leading to a larger $r_{\rm M}$.

Here, we note that, in the models adopted in the present study, $r_{\rm M}$ does not depend significantly on f. Therefore, $\dot{L}_{\rm EM}/\dot{M}_{\rm in}$ is not so sensitive to f. Simulations with a large $B_{\rm tot}$ and a small $\dot{M}_{\rm in}$, where $r_{\rm M}$ clearly depends on the magnetic field configuration, would clarify the dependence of $\dot{L}_{\rm EM}/\dot{M}_{\rm in}$ on f.

3.3. Radiation Flux

In Figure 8, we present the dependence of the radiation flux on f and ρ_0. The color shows the norm of the radiation flux in the poloidal direction $2\pi F^{(p)} r^2 \sin\theta$, where $F^{(p)} = \sqrt{(R^{(r)}_{(t)})^2 + (R^{(\theta)}_{(t)})^2}$. Vectors are the radiation flux vectors in the poloidal direction measured in the static observer's frame. It is evident that a powerful radiation flux emanates from the base of the accretion column or belt. Although not shown in this figure, in all models, $-2\pi r^2 \sin\theta \times R^r_t$ measured at the outer boundary has a peak near the rotation axis ($\theta < 30°$, $150° < \theta$). This means that the radiation from the accretion column and belt is collimated by the accretion flows and/or outflows (A. King et al. 2017; H. R. Takahashi & K. Ohsuga 2017; D. Abarca et al. 2021; A. Inoue et al. 2023).

In the following paragraphs, we explain the reason for $L_{\rm rad}^{\rm upper} \sim L_{\rm rad}^{\rm lower}$ (see Table 2). In models `D_d001`, `DQ_d001`, and `QD_001`, the same amount of the radiation energy is radiated from the accretion column toward the upper and lower hemispheres (see Appendix B). For example, in model `D_d001`, the radiation flux along the z-axis intensifies due to the radiation from the accretion column base toward $\theta = 0°$ (sometime called the polar beam; see, e.g., J. E. Trümper et al. 2013; S. B. Kobayashi et al. 2023). In addition, the radiation from the accretion column base toward the equator also creates the enhanced radiation flux towards the lower right direction for $r \lesssim 40$ km. The direction of the enhanced flux gradually changes, resulting in the radiation flux along the axis of $\theta = 180°$ for $r \gtrsim 100$ km. In this way, despite the formation of the accretion column at only one pole, $L_{\rm rad}^{\rm upper} \sim L_{\rm rad}^{\rm lower}$ is achieved. The resulting distribution of the radiation flux in models `DQ_d001` and `QD_d001` has almost the same trend as in model `D_d001`. The bending of the radiation flux direction would be attributed to scattering by electrons in the accretion flow. This can be inferred from the fact that the direction of the radiation energy transport is more curved than would be expected from geodesics.

In models `D_d01` and `DQ_d01`, the radiation flux exhibits symmetry with respect to the equator, due to the nearly equatorial symmetry of the accretion flow. Thus, $L_{\rm rad}^{\rm upper} \sim L_{\rm rad}^{\rm lower}$ holds. The same amount of radiation energy is radiated from the accretion belt located at the equator toward the upper and lower hemispheres in models `Q_d001`, `QD_d01`, and `Q_d01`. This results in $L_{\rm rad}^{\rm upper} \sim L_{\rm rad}^{\rm lower}$. Although the accretion column also exists in models `QD_d01` and `Q_d01`, the radiation from the accretion belt is more powerful than that from the accretion column. In addition, the outward radiation flux prominent at $\theta \sim 45°$ and 135° appears in models with $\rho_0 = 0.1\,{\rm g\,cm^{-3}}$. This originates from the radiation from the accretion column and/or belt toward the less dense region ($10\,{\rm km} \lesssim r \lesssim 20\,{\rm km}$, $45° \lesssim \theta \lesssim 135°$ for models `D_d01` and `DQ_d01`; $10\,{\rm km} \lesssim r \lesssim 12\,{\rm km}$, $45° \lesssim \theta \lesssim 60°$ for

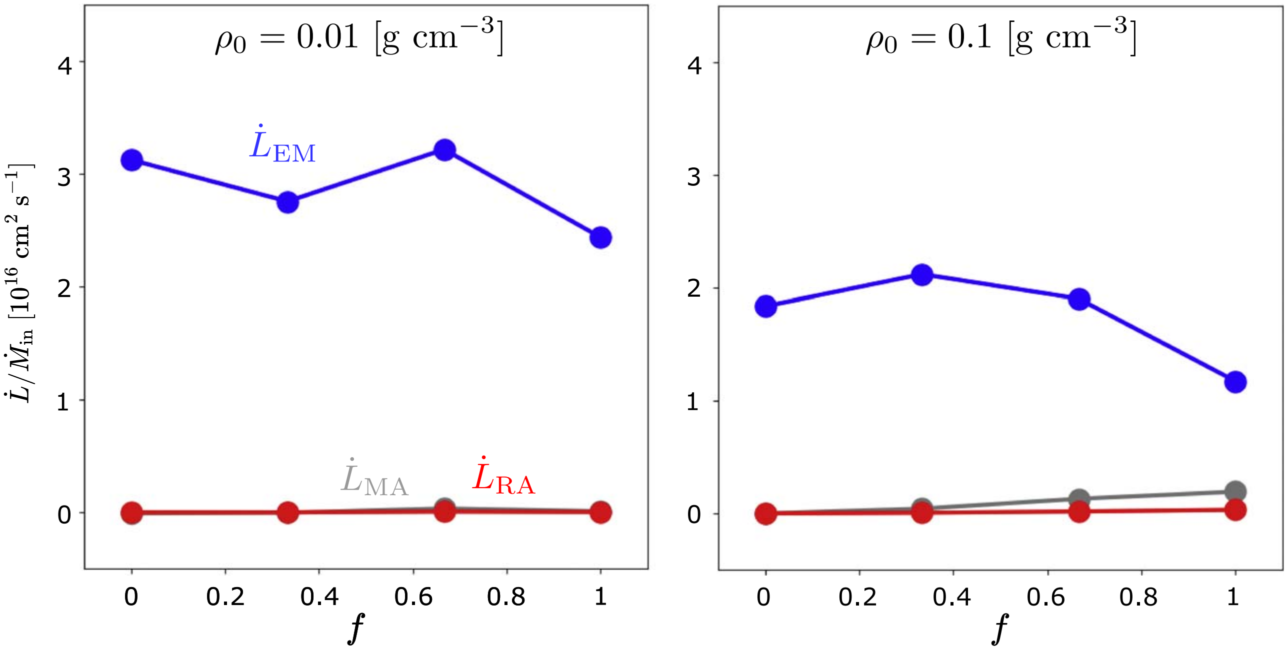

Figure 7. The angular momentum flux transferred to the NS normalized by the mass accretion rate (see the text).

model `QD_d01`; and $10\,{\rm km} \lesssim r \lesssim 12\,{\rm km}$, $45^\circ \lesssim \theta \lesssim 60^\circ$ for model `Q_d01`).

4. Discussion

4.1. The Magnetic Field of the NS in Swift J0243.6+6124

In this subsection, we apply our model to ULXPs Swift J0243.6+6124 and restrict the magnetic field strength of the NS. To summarize, the magnetic field strength 2×10^{13} G inferred from the CRSF observation would be originated from the quadrupole magnetic field. The dipole magnetic field strength $B_{\rm dip}$ would be less than 4×10^{12} G. These results do not contradict with the other observations, such as the thermal emission, pulse period, and spin-up rate.

We first discuss the case of $B_{\rm qua} \leqslant B_{\rm dip}$. Then, the dipole field is prominent in whole region, such that the quadrupole magnetic field would not affect the dynamics of the accretion flow. According to the discussion in Section 3.3 of A. Inoue et al. (2023), $B_{\rm dip}$ is estimated from three conditions: $r_{\rm M} < r_{\rm sph}$, $130\,\dot{M}_{\rm Edd} < \dot{M}_{\rm in} < 1200\,\dot{M}_{\rm Edd}$, and $r_{\rm NS} < r_{\rm M} < r_{\rm co}$. Here, $r_{\rm sph} = (3/2)(\dot{M}_{\rm in}/\dot{M}_{\rm Edd})r_{\rm g}$ is the spherization radius (N. I. Shakura & R. A. Sunyaev 1973; J. Poutanen et al. 2007), and $r_{\rm co} = [GMP^2/(2\pi)^2]^{1/3}$ is the corotation radius for the NS rotation. When $r_{\rm M} < r_{\rm sph}$, the outflows driven by the radiation force are launched from the accretion disk. Such outflows can explain the thermal emission observed in Swift J0243.6+6124 (L. Tao et al. 2019) when $130\,\dot{M}_{\rm Edd} < \dot{M}_{\rm in} < 1200\,\dot{M}_{\rm Edd}$. The condition of $r_{\rm M} < r_{\rm co}$ is required for the gas to accrete without being inhibited by the centrifugal force caused by the rotation of the magnetosphere (A. F. Illarionov & R. A. Sunyaev 1975). On the other hand, $r_{\rm M} > r_{\rm NS}$ is needed if the observed pulse originates from the accretion flows inside the magnetosphere. In the observations of Swift J0243.6+6124, the thermal emission is detected in two observations (Obs. 1 and 2), while is not detected in Obs. 3. The pulse period P is almost constant at 9.8 s, and the spin-up rate $\dot{P}$ is reported to be $\dot{P} = -2.22\times10^{-8}\,{\rm s\,s^{-1}}$ (Obs. 1), $\dot{P} = -1.75\times10^{-8}\,{\rm s\,s^{-1}}$ (Obs. 2), and $\dot{P} = -6.8\times10^{-9}\,{\rm s\,s^{-1}}$ (Obs. 3) (V. Doroshenko et al. 2018; X. Chen et al. 2021). Applying P and $\dot{P}$ in Obs. 1–3 to the three conditions noted above, we get $3\times10^{11}\,{\rm G} < B_{\rm dip} < 4\times10^{12}$ G. Since 2×10^{13} G is not included within this range, the observation of the CRSF cannot be explained. Thus, $B_{\rm qua} \leqslant B_{\rm dip}$ is ruled out.

When $B_{\rm qua} > B_{\rm dip}$, the CRSF would originate from the quadrupole magnetic field (i.e., $B_{\rm qua} = 2\times10^{13}$ G). In the following, we estimate the allowed range of $B_{\rm dip}$. First, we discuss the range of $B_{\rm dip}$ focusing only on Obs. 1. When $p_{\rm dip}(r_{\rm M}) \geqslant p_{\rm qua}(r_{\rm M})$ is satisfied, dipolar accretion flows occur (see Figure 4). Using Equations (24) and (27) from A. Inoue et al. (2023), this inequality can be rewritten as $B_{\rm dip} \geqslant B_{\rm dip}^{\rm trans}$. Here, $B_{\rm dip}^{\rm trans}$ is defined as

$$B_{\rm dip}^{\rm trans} = 8.6\times10^{11}\,[{\rm G}]\left(\frac{\alpha}{0.1}\right)^{-1/5}\left(\frac{B_{\rm qua}}{2\times10^{13}\,{\rm G}}\right)^{3/5}\left(\frac{M_{\rm NS}}{1.4M_\odot}\right)^{1/5} \times\left(\frac{r_{\rm NS}}{10\ {\rm km}}\right)^{-1/5}\left(\frac{P}{9.8\ {\rm s}}\right)^{-2/5}\left(\frac{\dot{P}}{-10^{-8}\ {\rm s\ s^{-1}}}\right)^{1/5}. \tag{22}$$

By substituting the observed values of $B_{\rm qua}$, $\dot{P}$, and P into Equation (22), we find that $B_{\rm dip}^{\rm trans} = 10^{12}$ G. Thus, the condition of $B_{\rm dip} \geqslant 10^{12}$ G is obtained. In addition to this, the condition of $2\times10^{10}\,{\rm G} < B_{\rm dip} < 5\times10^{12}$ G is also derived (for details, see A. Inoue et al. 2023). Combining both conditions, if $B_{\rm dip}$ is within the range of $10^{12}\,{\rm G} \leqslant B_{\rm dip} < 5\times10^{12}$ G, the observations in Obs. 1 can be explained by dipolar accretion flows.

On the other hand, when $p_{\rm dip}(r_{\rm M}) < p_{\rm qua}(r_{\rm M})$ ($B_{\rm dip} < B_{\rm dip}^{\rm trans} = 10^{12}$ G), quadrupolar accretion flows emerge. In this case, the conditions $r_{\rm M} < r_{\rm sph}$, $130\,\dot{M}_{\rm Edd} < \dot{M}_{\rm in} < 1200\,\dot{M}_{\rm Edd}$, and $r_{\rm NS} < r_{\rm M} < r_{\rm co}$ are all satisfied. First, regarding $\dot{M}_{\rm in}$, the spin-up rate is calculated using the equation $\dot{P} = \dot{M}_{\rm in} l_{\rm qua}(r_{\rm M}) P/(M_{\rm NS} l_{\rm NS})$

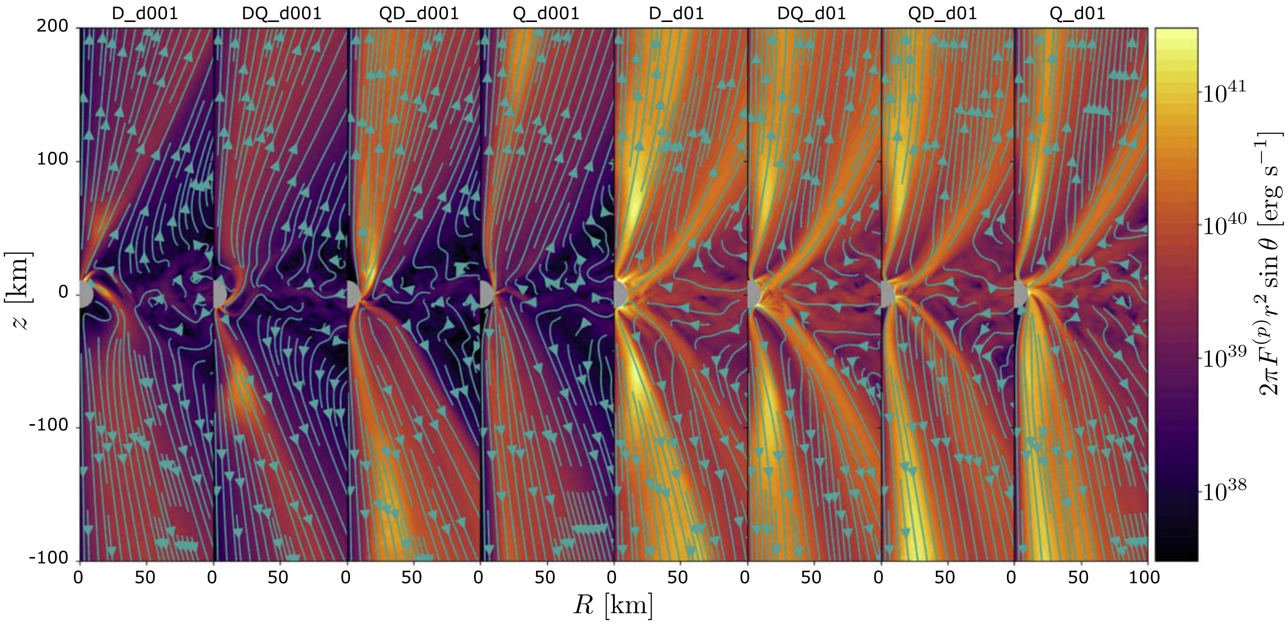

Figure 8. Color maps of the norm of the radiation flux in the poloidal direction. Vectors are the radiation flux vectors.

Table 3
$B_{\rm dip}$ Estimated from Each Observations

Obs. Name	Obs. 1	Obs. 2	Obs. 3
Dipolar accretion	10^{12} G $\leqslant B_{\rm dip} < 5 \times 10^{12}$ G	10^{12} G $\leqslant B_{\rm dip} < 4 \times 10^{12}$ G	8×10^{11} G $\leqslant B_{\rm dip} < 10^{14}$ G
Quadrupolar accretion	$B_{\rm dip} < 10^{12}$ G	$B_{\rm dip} < 10^{12}$ G	$B_{\rm dip} < 8 \times 10^{11}$ G
Combined	$B_{\rm dip} < 5 \times 10^{12}$ G	$B_{\rm dip} < 4 \times 10^{12}$ G	$B_{\rm dip} < 10^{14}$ G

(S. L. Shapiro & S. A. Teukolsky 1983):

$$\dot{P} = -8.9 \times 10^{-10} [\mathrm{s\ s^{-1}}] \left(\frac{\alpha}{0.1}\right)^{1/11} \left(\frac{\dot{M}_{\rm in}}{10\dot{M}_{\rm Edd}}\right)^{10/11} \times \left(\frac{B_{\rm qua}}{2 \times 10^{13}\ \mathrm{G}}\right)^{2/11} \left(\frac{r_{\rm NS}}{10^6\ \mathrm{cm}}\right)^{-14/11} \times \left(\frac{M_{\rm NS}}{1.4 M_\odot}\right)^{4/11} \left(\frac{P}{9.8\ \mathrm{s}}\right)^2, \tag{23}$$

where $l_{\rm NS}$ is the specific angular momentum of the NS. The reason $l_{\rm qua}$ is used here is that the quadrupole magnetic field is dominant at $R = r_{\rm M}$. From the observed values of $B_{\rm qua}$, $\dot{P}$, and P, $\dot{M}_{\rm in} = 340\dot{M}_{\rm Edd}$ is obtained using Equation (23), which meets the range of requirements. Moreover, the magnetospheric radius obtained from $p_{\rm rad} = p_{\rm qua}$ is 180 km, and since $r_{\rm sph} = 1100$ km, the first inequality ($r_{\rm M} < r_{\rm sph}$) is satisfied. Furthermore, because $r_{\rm co} = 7700$ km, the third inequality, $r_{\rm NS} < r_{\rm M} < r_{\rm co}$, is also satisfied.

As a result, combining both the cases of dipolar and quadrupolar accretion flows, the range of $B_{\rm dip}$ consistent with the observation of Obs.1 is $B_{\rm dip} < 5 \times 10^{12}$ G. Using the same manner explained above, the dipole magnetic field strength is restricted to $B_{\rm dip} < 4 \times 10^{12}$ G and $B_{\rm dip} < 10^{14}$ G for Obs. 2 and 3, respectively. In Table 3, we summarize the allowed range of $B_{\rm dip}$ separately for each observation (see the third row). The ranges of $B_{\rm dip}$ for the dipolar and quadrupolar accretion flow cases are also presented individually in the first and second rows, respectively. Assuming that the timescale of the decay of the NS's magnetic field is sufficiently long compared to the observation period, $B_{\rm dip} < 4 \times 10^{12}$ G is required in order to explain all three observations at the same time.

4.2. CRSF in Swift J0243.6+6124 and M51 ULX8

Here, we demonstrate that the line width of CRSF in Swift J0243.6+6124 and M51 ULX8 can be explained by the thermal motion of electrons inside accretion flows near the NS.

In our simulations, the gas temperatures of the accretion flows near the NS are $\sim 10^8$ K. Thus, we obtain the line width of $\sigma_{\rm cyc,e} = (E_{\rm cyc}/c)\sqrt{2kT/m_{\rm e}} \sim 19$ keV and $\sigma_{\rm cyc,p} = (E_{\rm cyc}/c)\sqrt{2kT/m_{\rm p}} \sim 0.44$ keV for $E_{\rm cyc} = 146$ keV (L.-D. Kong et al. 2022). The resulting $\sigma_{\rm cyc,e}$ is consistent with $\sigma_{\rm cyc}$ in Swift J0243.6+6124 ($\sigma_{\rm cyc} \sim$ 20–30 keV). On the other hand, the resulting $\sigma_{\rm cyc,p}$ is smaller than the observed $\sigma_{\rm cyc}$. A similar conclusion can be drawn for M51 ULX8. Assuming $E_{\rm cyc} = 4.5$ keV, $\sigma_{\rm cyc,e}$ would be 0.58 keV, which is consistent with the values suggested by observations (0.1 keV or 1.0 keV). However, $\sigma_{\rm cyc,p} \sim 0.013$ keV does not match the observed values. Thus, our simulations suggest that the CRSF in Swift J0234.6+6124 and M81 ULX8 originates from the resonant scattering of electrons. However, it should be noted that, if the gas temperature depends on the magnetic field strength of the NS, deviations from our results may occur, potentially altering the derived $\sigma_{\rm cyc,e}$ and $\sigma_{\rm cyc,p}$ values. Also, the optically thick accretion flows around the NS (i.e., the optically thick accretion curtain; see Figure 4) may obscure and thus lead to the disappearance of CRSFs from the observed spectrum (A. A. Mushtukov et al. 2017). Post-processing radiative transfer simulations are important to investigate the CRSF in detail.

4.3. Future Issues

Simulations of the NS with strong magnetic fields are needed in order to check the robustness of our conclusion. In this study, for numerical reasons, we consider an NS with a magnetic field strength of 4×10^{10} G, and the simulation results are extrapolated to the stronger magnetic field using the analytical solution of the spin-up rate. Whether Equations (20) and (21) hold for the strong magnetic field case should be confirmed directly by numerical simulations. Such simulations would also enable us to obtain the dependence of the spin-up rate on f (see Section 3.2). Recently, numerical methods that can solve the basic equations of GR-MHD stably in the high-magnetized region have been proposed (K. Parfrey & A. Tchekhovskoy 2017; D. Phillips & S. Komissarov 2023; K. Parfrey & A. Tchekhovskoy 2023; A. Chael 2024). In the future, we plan to implement such methods in our codes. In addition, simulations considering the reduced electron scattering opacity in the strong magnetic field are also left as important future work (X. Sheng et al. 2023). When the magnetic field strength exceeds 10^{13} G, the electron scattering cross section becomes smaller than the Thomson one. In this case, the radiation flux emergent from the side wall of the column would intensify, leading to a lower gas temperature inside the accretion column (A. A. Mushtukov et al. 2015). This results in the line width of the CRSF being narrower than estimated in Section 4.2.

We employ the M1 scheme in the present work. This scheme provides accurate radiation fields in optically thick regions, but when the system is optically thin and the radiation field is anisotropic, the M1 scheme can produce unphysical solutions (see, e.g., Y. Asahina et al. 2020). The accretion disk and outflows in our model are highly optically thick, so the adopted M1 closure is a good approximation to describe the radiation field. This approximation is, however, not appropriate near the rotation axis and in the low-density region within the magnetosphere. Therefore, to solve the structures near the neutron star more accurately, simulations in which the radiative transfer equation is directly solved are needed. Such simulations are left as very important future work (see, e.g., Y.-F. Jiang et al. 2014; K. Ohsuga & H. R. Takahashi 2016; Y. Asahina et al. 2020; L. Zhang et al. 2022; Y. Asahina & K. Ohsuga 2022).

Three-dimensional simulations of the super-Eddington accretion flows onto a rotating NS should be further investigated. In this study, we perform two-dimensional simulations of a non-rotating NS with its magnetic axis aligned with the disk's rotation axis. However, past numerical simulations showed that nonaxisymmetric modes are developed within the magnetosphere, due to the magnetic Rayleigh–Taylor instability (A. K. Kulkarni & M. M. Romanova 2008; S. Takasao et al. 2022; K. Parfrey & A. Tchekhovskoy 2023; P. Das & O. Porth 2024; A. Murguia-Berthier et al. 2024; Z. Zhu et al. 2024). In this case, the axisymmetric accretion columns would not form, indicating the absence of the polar beam. Furthermore, pulsations require that the NS rotates, and the magnetic axis is misaligned with the NS's rotation axis. Thus, we should take the nonaxisymmetric structure into account with three-dimensional simulations. In addition, the spin-down torque was detected in two ULXPs: M82 X-2 and Swift J0243.6+6124 (M. Bachetti et al. 2022; A. S. Karaferias et al. 2023; J. Liu 2024). This detection indicates that the NSs in these ULXPs are close to spin equilibrium. In this case, the centrifugal force due to the rotation of the NS's magnetosphere would affect the resultant spin-up rate (A. S. Karaferias et al. 2023) and the estimation of the magnetic field strength.

We plan to conduct post-processing radiative transfer simulations to obtain realistic radiation spectra. Our simulations show that the observed radiation spectra can be affected by Comptonization (see Section 3.1). The post-processing radiative transfer simulations let us estimate the radiation spectra including Comptonization. If we take the anisotropic electron scattering into account (see, e.g., H. Herold et al. 1982), the appearance of the CRSF can also be confirmed (see, Section 4.2). Additionally, these simulations might enable us to distinguish between the observational features of dipolar and quadrupolar accretion flows.

The investigation of the super-Eddington accretion flows, whose mass accretion rate gradually changes over time, is left as an important future work. In the present study, we examine the quasi-steady state of the super-Eddington accretion flows. However, in the observations of Swift J0243.6+6124, the observed luminosity changes across a wide range (see, e.g., C. A. Wilson-Hodge et al. 2018), which indicates that the mass accretion rate at the NS also changes. As the mass accretion rate increases, the resulting spin-up rate would also increase over time. To examine a more realistic situation, simulations in which the mass accretion rate changes over time are needed.

The large-scale structure of the accretion flow requires further investigation. In our simulations, the net mass accretion rate is almost constant (inflow–outflow equilibrium) within $r \lesssim 100$ km, and the quasi-steady outflows mainly originate from this region. Therefore, even if the inflow–outflow equilibrium region expands, our conclusion regarding the estimate of the NS magnetic field strength would remain unchanged. This is because the estimation of the NS magnetic field strength is based on the size of the photosphere in the outflow region, and while the expansion of the equilibrium region may lead to additional outflows, these are expected to flow primarily along the equatorial plane (T. Kitaki et al. 2021; S. Yoshioka et al. 2022). Consequently, the photosphere size would not change significantly, except near the equatorial plane. To accurately compute the large-scale accretion flows, long-term simulations with the initial torus placed further out will be required (see also recent simulations by D. Toyouchi et al. 2024).

5. Conclusion

In this study, we perform GR-RMHD simulations of super-Eddington accretion flows onto an NS with dipole and quadrupole magnetic fields. The super-Eddington accretion disks form outside the magnetospheric radius, and the optically thick outflows are launched from the disk surface via the radiation force. The inflows aligned with magnetic filed lines appear within the magnetospheric radius. Thus, the accretion columns near the NS's magnetic poles form when the dipole magnetic field is more prominent than the quadrupole magnetic field. For the case that the quadrupole magnetic field is dominant, the gas preferentially accretes along the equator, forming the accretion belt. In addition to the belt, the accretion column also forms when the mass accretion rate is high. In both cases, the angular momentum flux of the disk gas is converted into that of the electromagnetic field through the interaction between the gas and the NS's magnetic field lines around the magnetospheric radius. The inward angular momentum flux via the electromagnetic field finally causes the spin-up of the NS.

The radiation flux measured at the outer boundary of simulation domain is symmetric with respect to the equator, even if the asymmetric accretion flows form near the NS. The reason for this is that the radiation energy is transported to the opposite side across the equator. Based on our models, the observations in Swift J0243.6+6124, such as thermal emission, spin-up rate, spin periods, and CRSF, can be explained by an NS with $B_{\rm dip} \lesssim 4 \times 10^{12}$ G and $B_{\rm qua} \sim 2 \times 10^{13}$ G.

Acknowledgments

We would like to thank Takumi Ogawa for useful discussions. This work was supported by JSPS KAKENHI grant Nos. JP22KJ0368, JP24KJ0143 (A.I.), JP21H04488, JP18K03710 (K.O.), JP20H00156, JP24K00678 (H.R.T), JP18K13591, and JP23K03445 (Y.A.). A part of this research has been funded by the MEXT as "Program for Promoting Researches on the Supercomputer Fugaku" (Toward a unified view of the universe: from large-scale structures to planets, JPMXP1020200109; K.O., H.R.T., Y.A., and A.I.), and by the Joint Institute for Computational Fundamental Science (JICFuS; K.O.). Numerical computations were performed with computational resources provided by the Multidisciplinary Cooperative Research Program in the Center for Computational Sciences, University of Tsukuba, the Cray XC 50 at the Center for Computational Astrophysics (CfCA) of the National Astronomical Observatory of Japan (NAOJ), and the FUJITSU Supercomputer PRIMEHPC FX1000 and FUJITSU Server PRIMERGY GX2570 (Wisteria/BDEC-01) at the Information Technology Center, The University of Tokyo.

Appendix A
Radiative Shock

Here, we explain the radiative shock structure arising above the NS surface. In Figures 9 and 10, the density-weighted θ-averages of various quantities are plotted as functions of r. The values at $t = 32{,}420 t_{\rm g}$ are represented by dashed lines, while the time-averaged values are shown by solid lines. Here, we adopt $c_{\rm s} = \sqrt{p_{\rm rad}/\rho}$ as the sound speed, since $p_{\rm rad} \gg p_{\rm gas}$ inside the accretion flows. We note that, in all models, $p_{\rm mag}$ for $r \lesssim r_{\rm M}$ is greater than $p_{\rm rad}$, indicating that the accretion flows inside the magnetosphere are magnetically confined. In the models with a low rate of mass accretion ($\rho_0 = 0.01$ g cm^{-3}), the radiative shock structure is clearly seen. The discontinuity appears at $r \sim 15$ km for model `D_d001`, $r \sim 17$ km for model `DQ_d001`, $r \sim 15$ km for model `QD_d001`, and $r \sim 13$ km for model `Q_d001`. In the post-shock region, the accreting gas is decelerated by the outward radiation force. Thus, $-v^{(r)}$ in the post-shock region is smaller than that in pre-shock region. On the other hand, such a shock structure cannot be seen in the models with a high rate of mass accretion ($\rho_0 = 0.1$ g cm^{-3}). In these models, the infalling velocity for $r < r_{\rm M}$ is much smaller than the freefall velocity in spite of u_ϕ being smaller than the Keplerian angular momentum. The reason for this is that the shock surface reaches the accretion disk, and the outward radiation force keeps the infalling velocity small. The shock structure explained above depends on time. Therefore, the discontinuities of these quantities are smoothed out in the time-averaged profile.

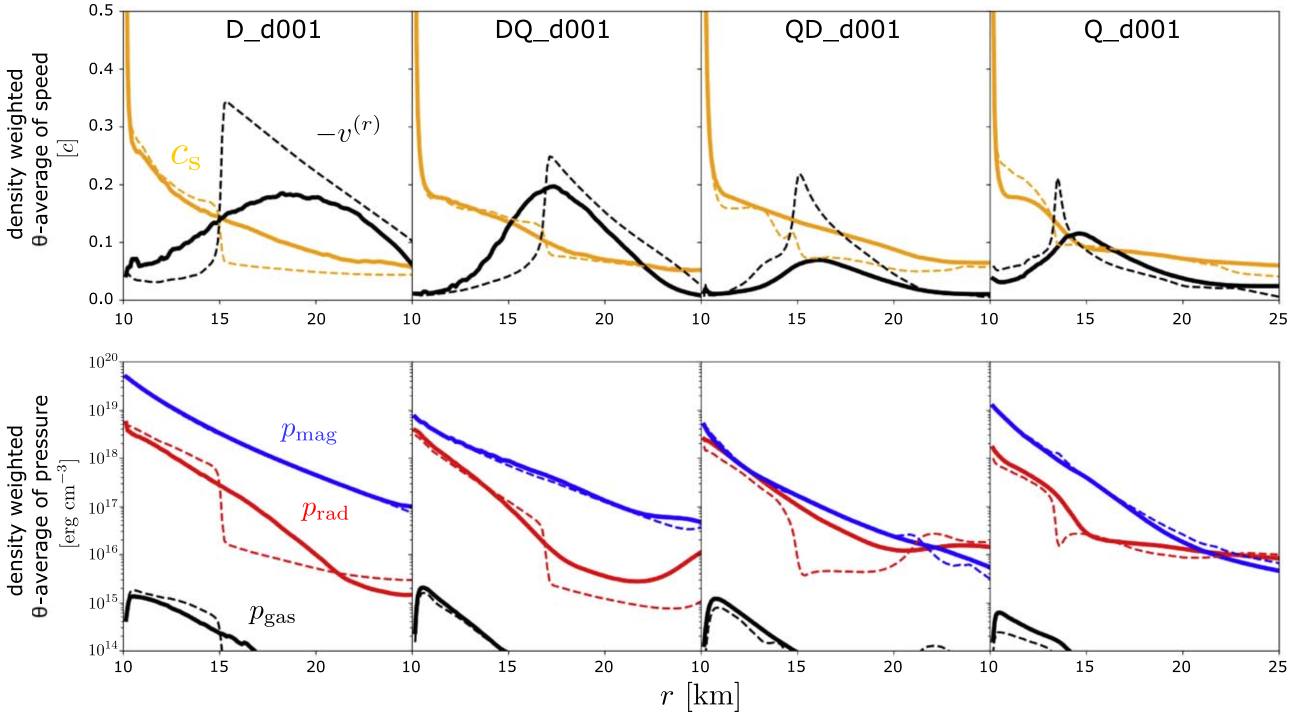

Figure 9. The radial profile of the infalling velocity, sound speed, radiation pressure, gas pressure, and radiation pressure for models of $\rho = 0.01$ g cm^{-3}.

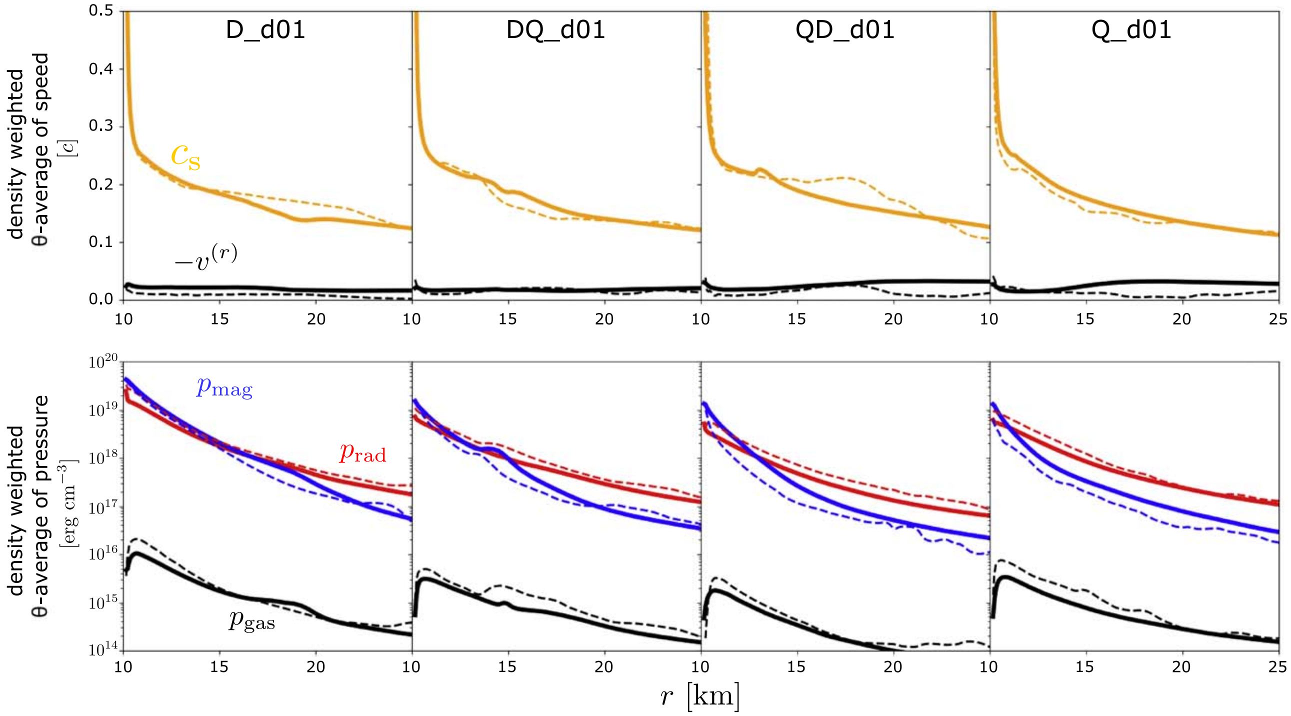

Figure 10. Same as Figure 9, but the case of $\rho = 0.1$ g cm^{-3}.

Appendix B
Radiation from the Accretion Columns

In our simulations, the same amount of the radiation energy is radiated from the accretion column toward the side with small θ and the side with large θ. Figure 11 illustrates the radiation energy density near the NS with the radiation energy flux vectors $(-R^{(r)}_{(t)}, -R^{(\theta)}_{(t)})$. Here, vectors are depicted only in the region of $4\pi r^2 F^{(p)} > 10L_{\rm Edd}$. Due to the radiative shock arising above the NS surface, the radiation energy density is high inside the accretion column. The surface area of the region where $\bar{E}$ is large has a parabolic shape (Y. E. Lyubarskii & R. A. Syunyaev 1988; A. A. Mushtukov et al. 2015). Considerable radiation energy flux emanates from the side wall of the accretion column, and radiation toward the side with small θ changes direction near the rotation axis and goes radially. We estimate the radiative luminosity from the side wall of the column toward the side with small θ ($L^1_{\rm rad}$) and the side with large θ ($L^2_{\rm rad}$) using

$$L^1_{\rm rad} = -2\pi \int_{0^\circ}^{30^\circ} R_t^{\ r}|_{r=15\ {\rm km}} \sqrt{-g}\, d\theta, \tag{B1}$$

$$L^2_{\rm rad} = -2\pi \int_{10\ {\rm km}}^{20\ {\rm km}} R_t^{\ \theta}|_{\theta=50^\circ} \sqrt{-g}\, dr. \tag{B2}$$

Here, the surfaces adopted for integration are drawn with yellow lines in Figure 11. We get $L^1_{\rm rad} \sim 1.0 \times 10^{39}$ erg s^{-1} and $L^1_{\rm rad} \sim 1.4 \times 10^{39}$ erg s^{-1}, and thus $L^1_{\rm rad} \sim L^2_{\rm rad}$.

We should note that, although the radiative luminosity from the side wall of the column is 10 times greater than $\sim L_{\rm Edd}$, the outward radiative luminosity in the fluid frame $(\hat{L}_{\rm rad} = -4\pi r^2 R_{\hat{t}}^{\hat{r}})$ inside the column is kept $\sim L_{\rm Edd}$. Figure 12 shows the ρ^3-weighted θ-average of $\hat{L}_{\rm rad}$ as a function of radius. We can see that the resulting luminosity is almost $\sim L_{\rm Edd}$ for 11 km $\lesssim r \lesssim$ 14 km. At $r \sim 15$ km, $\hat{L}_{\rm rad}$ has a peak due to the radiative shock. The large $\hat{L}_{\rm rad}$ near the NS's surface would be attributed to the boundary at which the gas is swallowed by the NS but the energy is not swallowed by the NS.

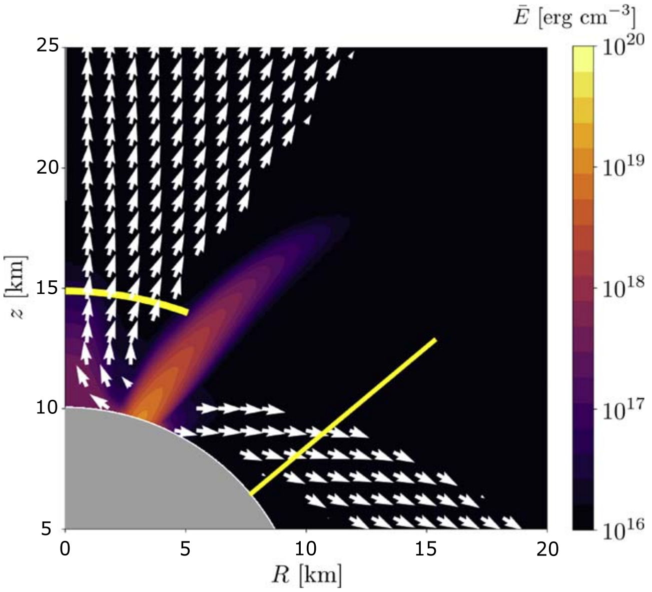

Figure 11. Color map of the time-averaged radiation energy density. Vectors are the radiation energy flux vectors in the region of $4\pi r^2 F^{(p)} > 10L_{\rm Edd}$. Yellow lines represent the surface area adopted for calculating $L^1_{\rm rad}$ and $L^2_{\rm rad}$.

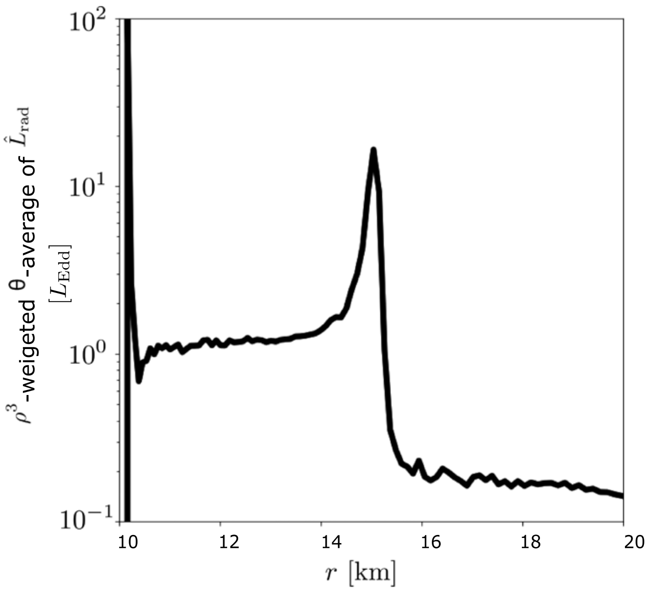

Figure 12. Radial profile of the density-weighted θ-average of radiative luminosity in the fluid frame. Here, we adopt the snapshot at $t = 32{,}420\, t_{\rm g}$.

ORCID iDs

Akihiro Inoue https://orcid.org/0000-0002-0700-2223
Ken Ohsuga https://orcid.org/0000-0002-2309-3639
Hiroyuki R. Takahashi https://orcid.org/0000-0003-0114-5378
Yuta Asahina https://orcid.org/0000-0003-3640-1749
Matthew J. Middleton https://orcid.org/0000-0002-8183-2970

References

Abarca, D., Parfrey, K., & Kluźniak, W. 2021, ApJL, 917, L31
Abolmasov, P., & Lipunova, G. 2023, MNRAS, 524, 4148
Asahina, Y., & Ohsuga, K. 2022, ApJ, 929, 93
Asahina, Y., Takahashi, H. R., & Ohsuga, K. 2020, ApJ, 901, 96
Bachetti, M., Harrison, F. A., Walton, D. J., et al. 2014, Natur, 514, 202
Bachetti, M., Heida, M., Maccarone, T., et al. 2022, ApJ, 937, 125
Balbus, S. A., & Hawley, J. F. 1991, ApJ, 376, 214
Basko, M. M., & Sunyaev, R. A. 1976, MNRAS, 175, 395
Brice, N., Zane, S., Turolla, R., & Wu, K. 2021, MNRAS, 504, 701
Brightman, M., Harrison, F. A., Fürst, F., et al. 2018, NatAs, 2, 312
Chael, A. 2024, MNRAS, 532, 3198
Chen, X., Wang, W., & Tong, H. 2021, JHEAp, 31, 1
Colbert, E. J. M., & Mushotzky, R. F. 1999, ApJ, 519, 89
Das, P., & Porth, O. 2024, ApJL, 960, L12
Das, P., Porth, O., & Watts, A. L. 2022, MNRAS, 515, 3144
Doroshenko, V., Tsygankov, S., & Santangelo, A. 2018, A&A, 613, A19
Doroshenko, V., Zhang, S. N., Santangelo, A., et al. 2020, MNRAS, 491, 1857
Eksi, K. Y., Andac, İ, Cıkıntoglu, S., et al. 2015, MNRAS, 448, L40
Fabrika, S. N., Atapin, K. E., Vinokurov, A. S., & Sholukhova, O. N. 2021, AstBu, 76, 6
Fishbone, L. G., & Moncrief, V. 1976, ApJ, 207, 962
Fragile, P. C., Etheridge, S. M., Anninos, P., Mishra, B., & Kluźniak, W. 2018, ApJ, 857, 1
Fürst, F., Walton, D. J., Harrison, F. A., et al. 2016, ApJL, 831, L14
Gladstone, J. C., Roberts, T. P., & Done, C. 2009, MNRAS, 397, 1836
Herold, H., Ruder, H., & Wunner, G. 1982, A&A, 115, 90
Illarionov, A. F., & Sunyaev, R. A. 1975, A&A, 39, 185
Inoue, A., Ohsuga, K., & Kawashima, T. 2020, PASJ, 72, 34
Inoue, A., Ohsuga, K., Takahashi, H. R., & Asahina, Y. 2023, ApJ, 952, 62
Israel, G. L., Belfiore, A., Stella, L., et al. 2017a, Sci, 355, 817
Israel, G. L., Papitto, A., Esposito, P., et al. 2017b, MNRAS, 466, L48
Jiang, Y.-F., Stone, J. M., & Davis, S. W. 2014, ApJ, 796, 106
Kaaret, P., Feng, H., & Roberts, T. P. 2017, ARA&A, 55, 303
Kanno, Y., Harada, T., & Hanawa, T. 2013, PASJ, 65, 72
Karaferias, A. S., Vasilopoulos, G., Petropoulou, M., et al. 2023, MNRAS, 520, 281
Kawashima, T., Mineshige, S., Ohsuga, K., & Ogawa, T. 2016, PASJ, 68, 83
Kawashima, T., & Ohsuga, K. 2020, PASJ, 72, 15
King, A., Lasota, J.-P., & Kluzniak, W. 2017, MNRAS, 468, L59
King, A., Lasota, J.-P., & Middleton, M. 2023, NewAR, 96, 101672
King, A. R., Davies, M. B., Ward, M. J., Fabbiano, G., & Elvis, M. 2001, ApJL, 552, L109
Kitaki, T., Mineshige, S., Ohsuga, K., & Kawashima, T. 2021, PASJ, 73, 450
Kobayashi, S. B., Noda, H., Enoto, T., et al. 2023, ApJ, 955, 124
Kong, L.-D., Zhang, S., Zhang, S.-N., et al. 2022, ApJL, 933, L3
Kulkarni, A. K., & Romanova, M. M. 2008, MNRAS, 386, 673
Levermore, C. D. 1984, JQSRT, 31, 149
Liu, J. 2024, ApJ, 961, 196
Long, M., Romanova, M. M., & Lovelace, R. V. E. 2007, MNRAS, 374, 436
Lyubarskii, Y. E., & Syunyaev, R. A. 1988, SvAL, 14, 390
Makishima, K., Kubota, A., Mizuno, T., et al. 2000, ApJ, 535, 632
Matsumoto, H., Tsuru, T. G., Koyama, K., et al. 2001, ApJL, 547, L25
McKinney, J. C., Tchekhovskoy, A., Sadowski, A., & Narayan, R. 2014, MNRAS, 441, 3177
Middleton, M. J., Brightman, M., Pintore, F., et al. 2019, MNRAS, 486, 2
Miller, J. M., Fabbiano, G., Miller, M. C., & Fabian, A. C. 2003, ApJL, 585, L37
Miller, J. M., Fabian, A. C., & Miller, M. C. 2004, ApJL, 614, L117
Murguia-Berthier, A., Parfrey, K., Tchekhovskoy, A., & Jacquemin-Ide, J. 2024, ApJL, 961, L20
Mushtukov, A. A., Suleimanov, V. F., Tsygankov, S. S., & Ingram, A. 2017, MNRAS, 467, 1202
Mushtukov, A. A., Suleimanov, V. F., Tsygankov, S. S., & Poutanen, J. 2015, MNRAS, 454, 2539
Mushtukov, A. A., Verhagen, P. A., Tsygankov, S. S., et al. 2018, MNRAS, 474, 5425
Ogawa, T., Mineshige, S., Kawashima, T., Ohsuga, K., & Hashizume, K. 2017, PASJ, 69, 33
Ohsuga, K. 2007, PASJ, 59, 1033
Ohsuga, K., & Mineshige, S. 2007, ApJ, 670, 1283
Ohsuga, K., & Takahashi, H. R. 2016, ApJ, 818, 162
Parfrey, K., Spitkovsky, A., & Beloborodov, A. M. 2016, ApJ, 822, 33
Parfrey, K., & Tchekhovskoy, A. 2017, ApJL, 851, L34
Parfrey, K., & Tchekhovskoy, A. 2024, ApJ, 975, 57
Phillips, D., & Komissarov, S. 2024, JPhCS, 2742, 012018
Pinto, C., & Walton, D. J. 2023, arXiv:2302.00006
Poutanen, J., Lipunova, G., Fabrika, S., Butkevich, A. G., & Abolmasov, P. 2007, MNRAS, 377, 1187
Ricarte, A., Narayan, R., & Curd, B. 2023, ApJL, 954, L22
Romanova, M. M., Ustyugova, G. V., Koldoba, A. V., & Lovelace, R. V. E. 2011, MNRAS, 416, 416
Sadowski, A., Lasota, J.-P., Abramowicz, M. A., & Narayan, R. 2016, MNRAS, 456, 3915
Sadowski, A., Narayan, R., McKinney, J. C., & Tchekhovskoy, A. 2014, MNRAS, 439, 503
Sadowski, A., Narayan, R., Tchekhovskoy, A., & Zhu, Y. 2013, MNRAS, 429, 3533
Sadowski, A., Narayan, R., Tchekhovskoy, A., et al. 2015, MNRAS, 447, 49
Shakura, N. I., & Sunyaev, R. A. 1973, A&A, 24, 337
Shapiro, S. L., & Teukolsky, S. A. 1983, Black Holes, White Dwarfs and Neutron Stars: The Physics of Compact Objects (New York: Wiley)
Sheng, X., Zhang, L., Blaes, O., & Jiang, Y.-F. 2023, MNRAS, 524, 2431
Takahashi, H. R., Mineshige, S., & Ohsuga, K. 2018, ApJ, 853, 45
Takahashi, H. R., & Ohsuga, K. 2017, ApJL, 845, L9
Takahashi, H. R., Ohsuga, K., Kawashima, T., & Sekiguchi, Y. 2016, ApJ, 826, 23
Takasao, S., Tomida, K., Iwasaki, K., & Suzuki, T. K. 2022, ApJ, 941, 73
Tao, L., Feng, H., Zhang, S., et al. 2019, ApJ, 873, 19
Thorne, K. S. 1981, MNRAS, 194, 439
Toyouchi, D., Hotokezaka, K., Inayoshi, K., & Kuiper, R. 2024, MNRAS, 532, 4826
Trümper, J. E., Dennerl, K., Kylafis, N. D., Ertan, Ü., & Zezas, A. 2013, ApJ, 764, 49
Tsygankov, S. S., Doroshenko, V., Mushtukov, A. A., Lutovinov, A. A., & Poutanen, J. 2018, MNRAS, 479, L134
Utsumi, A., Ohsuga, K., Takahashi, H. R., & Asahina, Y. 2022, ApJ, 935, 26
Watarai, K.-y., & Fukue, J. 1999, PASJ, 51, 725
Watarai, K.-y., Mizuno, T., & Mineshige, S. 2001, ApJL, 549, L77
Wilson-Hodge, C. A., Malacaria, C., Jenke, P. A., et al. 2018, ApJ, 863, 9
Yoshioka, S., Mineshige, S., Ohsuga, K., Kawashima, T., & Kitaki, T. 2022, PASJ, 74, 1378
Zhang, L., Blaes, O., & Jiang, Y.-F. 2022, MNRAS, 515, 4371
Zhang, L., Blaes, O., & Jiang, Y.-F. 2023, MNRAS, 520, 1421
Zhu, Z., Stone, J. M., & Calvet, N. 2024, MNRAS, 528, 2883